Harnessing DNA replication stress to target RBM10 deficiency in lung adenocarcinoma

Feras E. Machour[1], Enas Abu-Zhayia[1], Joyce Kamar[2], Alma Sophia Barisaac[1]
Itamar Simon[2], Nabieh Ayoub*[1]

[1]Department of Biology, Technion - Israel Institute of Technology, Haifa 3200003, Israel.
[2]Department of Microbiology and Molecular Genetics, Institute of Medical Research Israel-Canada, Faculty of Medicine, The Hebrew University, Jerusalem, Israel

*Corresponding author: Prof. Nabieh Ayoub, Faculty of Biology
Technion - Israel Institute of Technology
Haifa 3200003, Israel.
Tel: +972-4-8294232 Fax: +972-4-8225153
Email: ayoubn@technion.ac.il

Abstract (150 words)

The splicing factor RBM10 is frequently mutated in lung adenocarcinoma (LUAD) (9-25%). Most RBM10 cancer mutations are loss-of-function, correlating with increased tumorigenesis and limiting targeted therapy efficacy in EGFR-mutated lung cancer. Notably, therapeutic strategies leveraging RBM10 deficiency remain unexplored. Hence, we conducted RBM10 CRISPR-Cas9 synthetic lethality (SL) screen and identified ~250 RBM10 SL genes, including WEE1 kinase. WEE1 inhibition sensitized RBM10-deficient LUAD cells *in-vitro* and *in-vivo*. Mechanistically, we identified a splicing-independent role of RBM10 in promoting replication fork progression that underpins RBM10-WEE1 SL. Also, we revealed that RBM10 is associated with active replication forks, which is reliant on PRIM1, an enzyme synthesizing RNA primers for Okazaki fragments. Functionally, we demonstrated that RBM10 serves as an anchor for recruiting HDAC1 and facilitates H4K16 deacetylation to maintain replication fork stability. Collectively, our data revealed a hitherto unrecognized function of RBM10 in fine-tuning DNA replication, and provide therapeutic arsenal for targeting RBM10-deficient tumors.

Introduction

Lung cancer has the highest mortality rate among all types of cancer worldwide[1,2]. Non-small cell lung cancer (NSCLC) comprises 85% of all lung cancer cases and is subdivided into different subtypes including lung adenocarcinoma (LUAD) (40%)[3,4]. Most LUAD patients are diagnosed at advanced or metastatic stage, when treatment options are limited to surgery, chemotherapy, and few targeted therapies[4]. EGFR and KRAS are the most mutated oncogenes in LUAD amongst Asian (60%) and Caucasian (33%) cohorts, respectively[5,6]. Accordingly, several targeted therapies, including EGFR and KRAS inhibition, are currently used in the clinic for the treatment of advanced stages of LUAD harboring KRAS and EGFR mutations[7,8]. However, effective treatment of LUAD remains elusive due to the genetic diversity of the disease and the development of therapeutic resistance. Thus, there is a critical need for identifying new therapeutic targets for personalized treatment of LUAD. Interestingly, RNA-binding proteins are broadly dysregulated in human cancers including LUAD and play a key role in carcinogenesis and metastatic progression[9–17]. Therefore, alterations in RNA-binding proteins might provide excellent therapeutic targets for treating lung cancer. One very attractive and yet unexplored therapeutic target is the RNA-binding protein, RBM10.

RBM10 is mapped to the X chromosome[18], and its mutations cause TARP syndrome, an X-linked disorder that leads to pre- and postnatal lethality in affected males[19–25]. RBM10 is a key regulator of alternative splicing that mainly promotes exon skipping of its target genes[26–32]. Also, RBM10 impacts chromatin structure and chromosome segregation independently of its splicing activity[33–36]. Mounting evidence show that RBM10 acts as a tumor suppressor, as its depletion increases cell proliferation and enhances mouse xenograft tumor formation[6,29,32,37–42]. Concordantly, RBM10 overexpression suppresses LUAD tumor growth *in vivo*[6,43]. RBM10 exerts its tumor suppressive activity through various mechanisms[29,40,44]. For example, it was shown that RBM10 inhibits cell proliferation and tumor growth through alternative splicing regulation of NUMB and EIF4H genes[6,32,39]

RBM10 is the most mutated splicing factor in LUAD and is mutated in 9% of all LUAD cases[5]. Strikingly, this percentage rises to 21% in invasive subtypes of LUAD, and 25% in multiple primary LUAD[45,46]. Moreover, RBM10 mutation rate is higher than KRAS and TP53 mutations in early stages of LUAD in patients from Asian origin[47,48]. Most RBM10 mutations in LUAD correspond to loss-of-function and are associated with poor survival[49,50]. Notably, RBM10 mutations mostly co-occur with EGFR and KRAS mutations and were shown to reduce the efficiency of tyrosine kinase inhibitors (TKIs) in LUAD patients harboring EGFR

68 mutations[6,51]. Altogether, these findings highlight the urgency of therapeutic targeting of
69 RBM10 deficiency in LUAD.
70 Herein, we performed a genome-wide CRISPR-Cas9 synthetic lethality (SL) screen in isogenic
71 LUAD cell line harboring RBM10 cancer mutation and identified ~250 high-scoring RBM10
72 SL genes, including WEE1 and Aurora A kinases. We show that pharmacological inhibition of
73 WEE1 selectively sensitizes RBM10-deficient LUAD cells, including patient-derived cells
74 harboring RBM10 cancer mutations, *in vitro* and in mouse xenograft model, and this effect was
75 further exacerbated when combined with Aurora A inhibition. Mechanistically, we identified
76 a splicing-independent role of RBM10 in promoting DNA replication fork progression that
77 underpins RBM10-WEE1 SL. We also show that RBM10 is associated with active replication
78 forks, which is contingent upon PRIM1, an enzyme responsible for synthesizing RNA primers
79 of Okazaki fragments. Functionally, we demonstrated that RBM10 loss disrupts the
80 localization of HDAC1 at replication forks, leading to elevated levels of H4K16ac, which
81 destabilizes the replication fork and induces replication stress. Collectively, our data revealed
82 a hitherto unrecognized function of the RNA-binding protein RBM10 in fine-tuning DNA
83 replication, and identify DNA replication stress as an SL pathway with RBM10 loss. Moreover,
84 we provide a repertoire of RBM10 SL targets that can be harnessed therapeutically to eradicate
85 RBM10-deficient tumors with immediate clinical applicability.

86 **Results**

87 **Genome-wide CRISPR-Cas9 screen reveals synthetic lethal partners of RBM10 in LUAD**
88 **cells**

89 Given that RBM10 is one of the most mutated genes in LUAD, we sought to identify genetic
90 vulnerabilities to RBM10 loss. To achieve this, we conducted an unbiased genome-scale
91 CRISPR-Cas9 SL screen in LUAD HCC827 cell line. HCC827 cells harbor a common
92 oncogenic deletion in EGFR (E746-A750), and are a pertinent model to screen for genetic
93 vulnerabilities to RBM10 loss since RBM10 and EGFR mutations often co-occur in LUAD,
94 and RBM10 loss was shown to limit the response to common EGFR-targeted therapy[6,51].
95 Therefore, we sought to generate isogenic HCC827 cells stably expressing comparable levels
96 of flag-Cas9 endonuclease and differ only in the status of RBM10. Toward this end, we
97 designed a sgRNA targeting RBM10 exon 2 to introduce a frameshift mutation V176Rfs*, that
98 exhibits a complete absence of RBM10 protein, while constitutively expressing Cas9 protein
99 (HCC827-Cas9$^{RBM10\text{-}KO}$) (Fig. 1a and Supplementary Fig. 1a,b). Interestingly, the introduced
100 mutation closely resembles a previously characterized LUAD cancer mutation E177* that

101 abrogates RBM10 splicing activity and leads to RBM10 protein loss[50]. Notably, HCC827-
102 Cas9$^{RBM10-KO}$ cells exhibit an increase in exon inclusion of RBM10 splicing targets NUMB and
103 EIF4H, phenocopying the defective splicing phenotype of RBM10-deficient LUAD[6,32] (Fig.
104 1b and Supplementary Fig. 1c).
105 Next, we conducted a genome-scale CRISPR-Cas9 SL screen in the isogenic HCC827-Cas9^{WT}
106 and HCC827-Cas9$^{RBM10-KO}$ using the TKOv1 sgRNA library, which contains 91,320 sgRNAs
107 targeting 17,232 protein-coding genes[52]. Cells were collected at 0 and 15 days following
108 TKOv1 library transduction and subjected to next-generation sequencing to measure sgRNA
109 abundance (Supplementary Fig. 1d). To identify bona fide RBM10 SL genes that are
110 selectively essential in RBM10-KO cells, we analyzed the screen results using three distinct
111 scoring methods: Bayesian Analysis of Gene Essentiality (BAGEL2)[53], Model-Based Analysis
112 of Genome-wide CRISPR-Cas9 Knockout (MAGeCK)[54], and CRISPR Count Analysis
113 (CCA)[55]. These methods unveiled 210, 280, and 357 RBM10 SL genes, respectively (Fig. 1c,
114 Supplementary Fig. 1e, and Supplementary Table 1). Of note, a comparative analysis of
115 RBM10 SL genes among the three different assays, revealed 60 RBM10 SL genes that are
116 common to all three analysis methods (Supplementary Fig. 1f). Gene-set enrichment analysis
117 revealed significant enrichment of several pathways including mRNA splicing, cell cycle
118 checkpoints, S-phase, and DNA replication (Fig. 1d).

119 To functionally validate the screen results, we conditionally knocked-down 5 candidate
120 RBM10 SL genes annotated to various enriched pathways (SF3B1, WAPAL, WEE1, AURKA,
121 PEX10), and 2 common essential (XRN2, LSM7), followed by clonogenic survival assay.
122 While depletion of common essential genes had a similar effect in inhibiting the proliferation
123 of both parental and RBM10-KO cells, depletion of candidate RBM10 SL genes selectively
124 inhibited the proliferation of HCC827-Cas9$^{RBM10-KO}$ cells, confirming successful identification
125 of bona-fide RBM10 SL genes (Fig. 1e and Supplementary Fig. 1g).

126 Interestingly, several RBM10 SL genes, such as WAPAL, WEE1, CHEK1, ATRIP, and
127 MRE11, were identified using the three aforementioned scoring methods. These genes have
128 known functions in DNA replication stress response and replication fork protection, suggesting
129 DNA replication stress as a synthetic lethal pathway with RBM10 deficiency in LUAD (Fig.
130 1f). In support of this, RBM10 was previously identified as a candidate replication stress
131 response gene by a genome-wide siRNA screen[56], and a phosphorylation target of ATR[57].
132 Additionally, RBM10 was shown to interact with several proteins involved in DNA replication
133 and repair in fission yeast[36]. Fittingly, analysis of "The Cancer Genome Atlas" (TCGA[58])

mutation data from LUAD patients revealed that RBM10 deficiency is associated with increased tumor mutational burden and replication stress gene signature (Supplementary Fig. 1h,i). Collectively, these observations suggest a role of RBM10 in DNA replication and genomic stability.

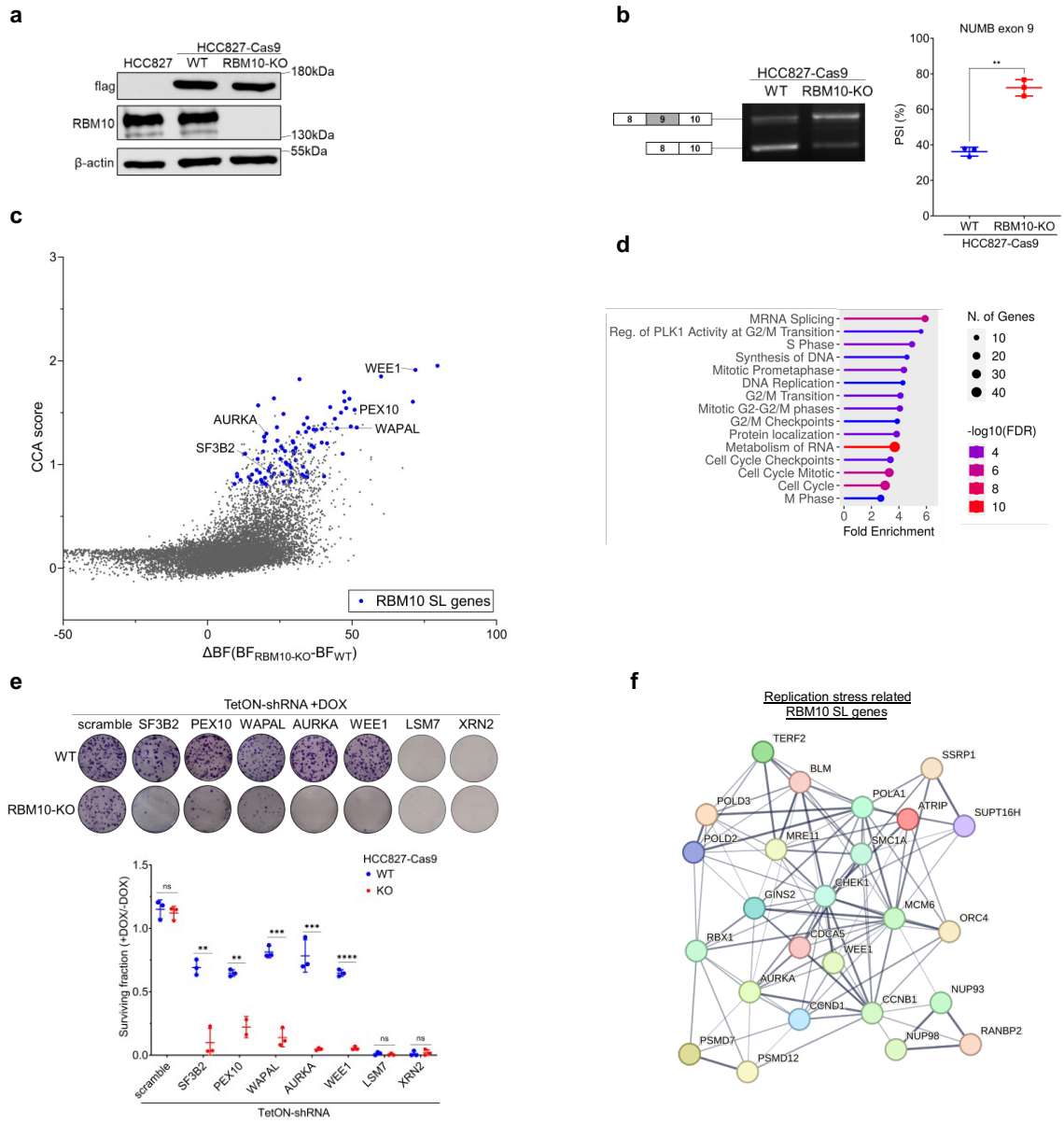

Figure 1: Genome-wide CRISPR-Cas9 screen reveals synthetic lethal partners of RBM10 in LUAD cells. (a) Immunoblot analysis for RBM10 and flag-Cas9 protein expression in isogenic RBM10-deficient HCC827 cells constitutively expressing flag-Cas9. β-actin is used as a loading control. The positions of molecular weight markers are indicated to the right. **(b)** RT-PCR analysis of NUMB exon 9 alternative splicing in parental (WT) and HCC827-Cas9$^{RBM10\text{-}KO}$ cells. RNA was isolated from the indicated cell lines and analyzed by RT-PCR using primers flanking NUMB exons 8-10. Left: Representative agarose gel image showing amplification of two NUMB variants that differ in exon 9 inclusion. Right: Precent-spliced-in

148 (PSI) quantification of NUMB exon 9 inclusion. Data are presented as mean ± s.d. (n=3).
149 Statistical significance was determined by unpaired t-test. ***$P<0.001$. **(c)** Results of CRISPR-
150 Cas9 SL screen in WT and HCC827-Cas9$^{RBM10-KO}$ cells performed in triplicates. CRISPR
151 Counts Analysis (CCA) score is plotted against the difference in gene essentiality score,
152 expressed as Bayes Factor (BF), between RBM10-KO cells and WT cells. RBM10 SL genes
153 are shown in blue. **(d)** Gene ontology analysis of RBM10 SL genes identified in the CRISPR-
154 Cas9 SL screen. **(e)** Clonogenic survival of WT and HCC827-Cas9$^{RBM10-KO}$ cells transduced
155 with inducible vector expressing either scramble shRNA or shRNA targeting the indicated
156 genes upon the addition of doxycycline (DOX). Top: Representative images of crystal violet
157 staining of the indicated cell lines treated with DOX. Bottom: Quantification of clonogenic
158 survival in DOX-treated cells normalized to untreated cells. Data are presented as mean ± s.d.
159 (n=3). Statistical significance was determined by unpaired t-test.
160 **$P<0.01$;***$P<0.001$;****$P<0.0001$. **(f)** STRING interaction network of RBM10 SL genes
161 involved in replication stress response and cell cycle. The thickness of the connecting line
162 indicates interaction confidence.
163

164 **RBM10 promotes DNA replication fork progression and replication stress response**

165 Herein, we sought to determine the impact of RBM10 loss on replication fork progression.
166 DNA fiber analysis showed that HCC827-Cas9$^{RBM10-KO}$ cells display a significant replication
167 fork slowdown, suggesting that RBM10 is required for proper fork progression (Fig. 2a).
168 Similar results were also observed in a second RBM10-KO clone (KO2) isolated from
169 HCC827-Cas9 cells, arguing against a clonal effect (Supplementary Fig. 2a). To confirm that
170 the effect of RBM10 loss on replication fork progression is not cell-line specific, and since
171 TP53 mutations often co-occur with RBM10 mutations in LUAD[58], we tested the effect of
172 RBM10 knockout on replication fork progression in p53-deficient LUAD cells NCI-H1299
173 (H1299$^{RBM10-KO}$) (Supplementary Fig. 2b,c). Results show that RBM10 loss in H1299 cells also
174 led to significant reduction in replication fork progression, suggesting that the effect of RBM10
175 on DNA replication is independent of common co-occurring mutations such as EGFR and
176 TP53 (Fig 2b). Immunostaining analysis revealed that replication fork slowdown upon RBM10
177 loss is accompanied by an increase in the levels of pRPA32-S33 and γH2AX, primarily
178 observed in S phase cells marked by EdU staining (Fig. 2c-e). Similarly, western blot analysis
179 demonstrated a significant increase in pRPA32-S33, pCHK1, and γH2AX in RBM10 knockout
180 (KO) cells synchronized at the S phase using a double-thymidine block (Supplementary Fig.
181 2d). Next, we investigated the effect of RBM10 loss on the recovery from hydroxyurea (HU)
182 induced replication stress. Results showed that RBM10-deficient cells display a significant
183 increase in replication stress and DNA damage markers after release from HU, with no
184 significant effect on replication fork restart (Fig. 2f and Supplementary Fig. 2e). Corollary to
185 this, RBM10-deficient cells are markedly more sensitive than RBM10-proficient cells to

186 increasing HU concentrations (Fig. 2g). Collectively, our results demonstrate that RBM10
187 fosters efficient DNA replication fork progression and fork recovery during replication stress.
188

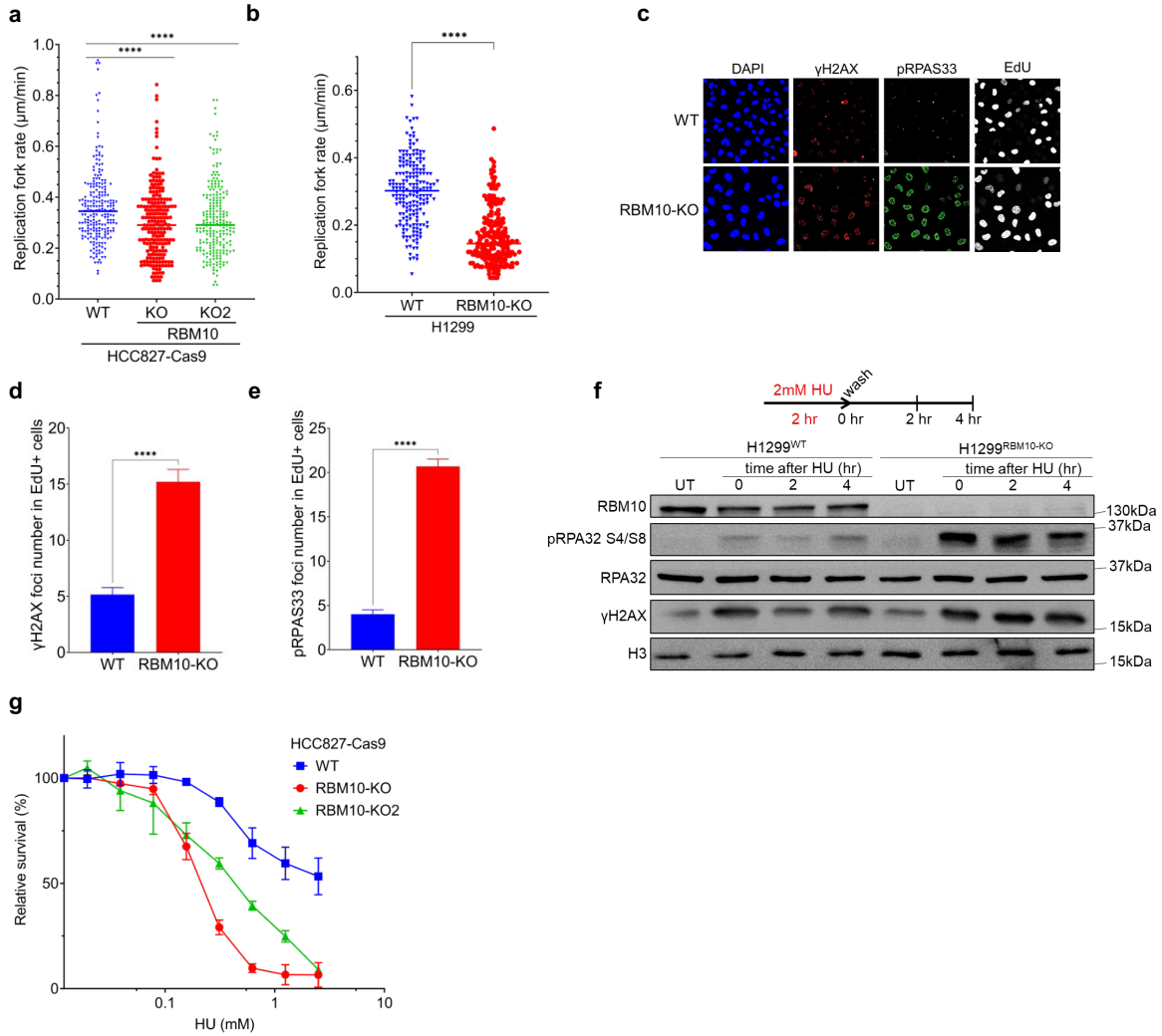

189
190
191 **Figure 2: RBM10 promotes DNA replication fork progression and replication stress**
192 **response. (a,b)** Replication fork speed measurement using DNA combing assay in WT and
193 RRBM10-KO HCC827 (a) or H1299 (b) cells. Horizontal bars represent mean value of
194 replication fork speed (n>200). Statistical significance was determined by Mann-Whitney test.
195 ****$P<0.0001$. **(c)** Representative immunofluorescence microscopy images of pRPA32-S33
196 and γH2AX foci in H1299^{WT} and H1299$^{RBM10\text{-}KO}$ cells. EdU is used to mark S-phase cells.
197 DAPI is used to stain nuclei. Scale bar, 20µm. **(d,e)** Quantification of γH2AX (d) and pRPA32-
198 S33 (e) foci in S-phase (EdU-positive) H1299^{WT} and H1299$^{RBM10\text{-}KO}$ cells. Data are presented
199 as mean foci number per nucleus ± SEM (n>200 cells) and representative of 3 independent
200 experiments. Statistical significance was determined by Mann-Whitney test. ****$P<0.0001$.
201 **(f)** H1299^{WT} and H1299$^{RBM10\text{-}KO}$ cells were treated with 2mM hydroxyurea (HU) for 2 hr and
202 subjected to immunoblot analysis at the indicated times after release from HU. Histone H3 is
203 used as a loading control. UT=untreated. The positions of molecular weight markers are
204 indicated to the right. **(g)** Short-term cell viability assay in parental (WT) and RBM10-KO
205 HCC827-Cas9 cells treated with increasing concentrations of HU. Data are presented as mean
206 ± s.d. (n=3).

207 **RBM10 is associated with active DNA replication fork in a PRIM1-dependent manner**
208 To gain molecular insights into the involvement of RBM10 in replication fork progression, we
209 first determined its sub-cellular localization. Biochemical fractionation revealed that RBM10
210 is enriched at the chromatin-bound fraction (Supplementary Fig. 3a), supporting the notion that
211 RBM10 has a direct role in regulating replication fork progression. To further substantiate this,
212 cells expressing RBM10 fused to EGFP were subjected to GFP-trap followed by mass
213 spectrometry (MS) analysis to map RBM10 interactome. Results revealed 410 RBM10-
214 interacting proteins annotated to several pathways, most notably the spliceosome, consistent
215 with RBM10 function in alternative splicing, as well as DNA replication. (Fig. 3a and
216 Supplementary Table 2). Intriguingly, we revealed that RBM10 interacts with replication fork
217 components and proteins involved in replication stress response (Supplementary Fig. 3b). Next,
218 we validated the authenticity of RBM10 interactome and showed that RBM10 interacts with
219 MCM5, PCNA, HDAC1, PARP1, and RAD51 (Fig. 3b).
220 To further substantiate RBM10 interaction with replication forks, first we confirmed the
221 interaction between endogenous RBM10 and PCNA in LUAD cells (Supplementary Fig. 3c).
222 Second, we tested whether RBM10 is associated with active replication forks in cells using
223 proximity ligation assay (PLA). Results showed that RBM10 is in close proximity to PCNA
224 (Fig. 3c). Moreover, PLA combined with EdU click chemistry revealed that RBM10 is
225 associated with EdU-labelled nascent DNA, marking sites of active DNA replication (Fig. 3d).
226 Collectively, our data provide firm evidence that RBM10 interacts with active DNA replication
227 forks under native conditions.
228 Next, we aimed to gain molecular insights into the mechanism governing the association of
229 RBM10 with DNA replication forks. Given that RBM10 is a well-established RNA-binding
230 protein, we hypothesized that its binding to RNA molecules facilitates its association with
231 chromatin. To explore this hypothesis, we treated cells with RNase A followed by chromatin
232 fractionation. Our results revealed that RNase A treatment profoundly disrupts RBM10
233 association with chromatin (Supplementary Fig. 3d). Consistent with this observation, an
234 RBM10 deletion mutant lacking the first ZnF domain ($RBM10^{\Delta ZNF1}$), known to bind RNA
235 molecules[59,60], lost its association with active DNA replication forks, as determined by PLA
236 (Fig. 3e). Remarkably, a recent work has shown that PRIM1, an enzyme involved in
237 synthesizing RNA primers for Okazaki fragments, facilitates the recruitment of 53BP1 to DNA
238 replication forks[61]. Hence, we investigated whether a similar scenario exists with RBM10. Our
239 results reveal that siRNA knockdown of PRIM1 pronouncedly diminishes the association of

RBM10 with active DNA replication forks similar to 53BP1 (Fig. 3f and Supplementary Fig. 4a,b). Collectively, these findings robustly support the notion that Okazaki RNA primers play a pivotal role in mediating the recruitment of RBM10 to replication forks.

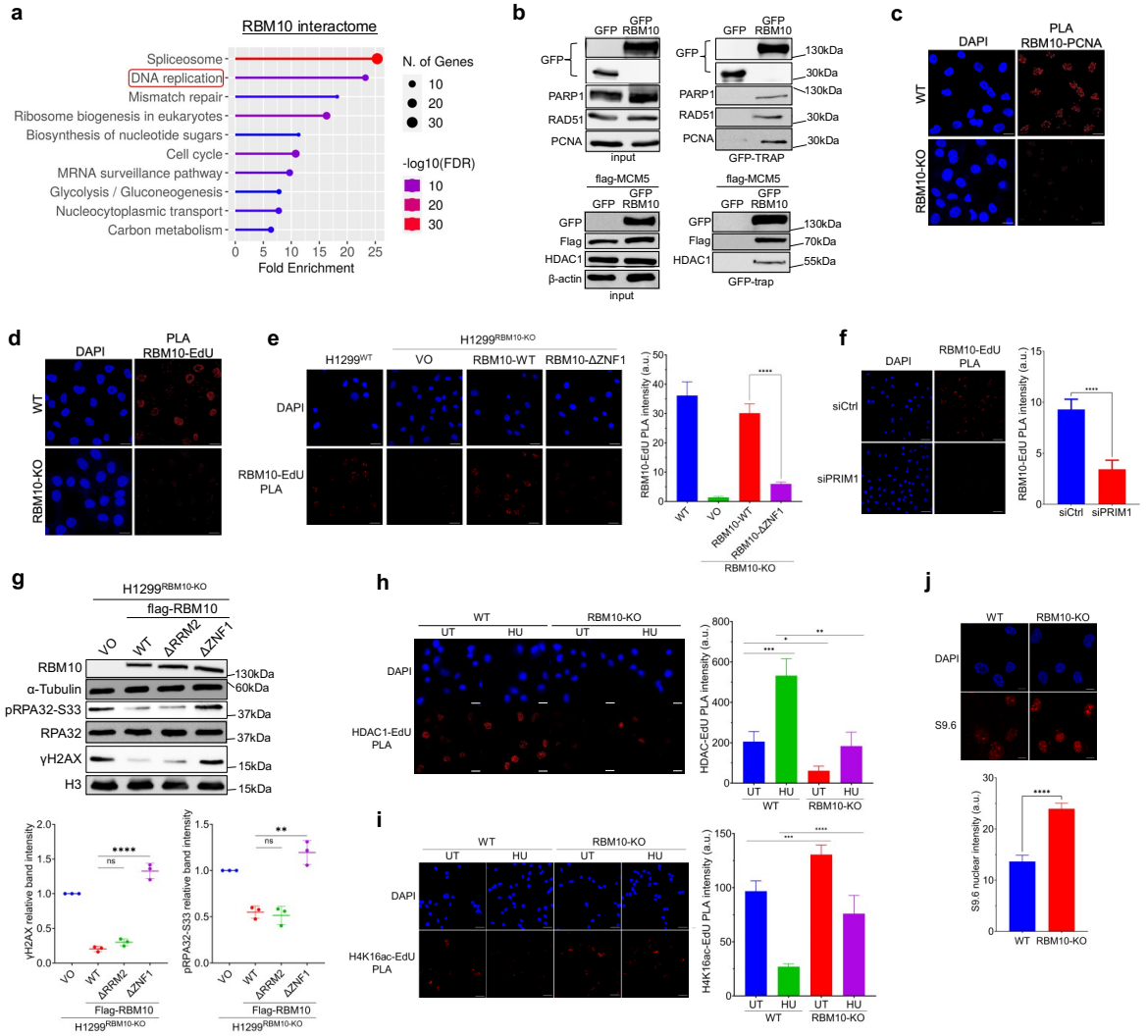

Figure 3: PRIM1-dependent RBM10 association with DNA replication forks promotes HDAC1 recruitment to limit replication stress. (a) Gene ontology analysis of RBM10 interactome in unchallenged cells as identified by GFP-trap followed by mass spectrometry analysis. **(b)** HEK293T cells expressing EGFP-RBM10 or EGFP only were subjected to GFP-trap followed by immunoblot analysis using the indicated antibodies. Bottom: GFP-trap was performed on HEK293T cells additionally expressing Flag-MCM5. The positions of molecular weight markers are indicated to the right. **(c,d)** Representative immunofluorescence microscopy images of RBM10:PCNA (c) and RBM10:EdU-biotin (d) proximity ligation assay (PLA) foci in H1299^{WT} and H1299$^{RBM10\text{-}KO}$ cells. Scale bar, 20µm. **(e)** Left: Representative immunofluorescence microscopy images of RBM10:EdU-biotin PLA in H1299$^{RBM10\text{-}KO}$ expressing Flag-RBM10^{WT}, Flag-RBM10$^{\Delta ZNF1}$, or vector only (VO). DAPI is used to stain nuclei. Scale bar, 20µm. Right: Quantification of RBM10-EdU-biotin PLA intensity per nucleus. Data are presented as mean PLA intensity per nucleus ± SEM (n>300 cells). Statistical significance was determined by Mann-Whitney test. ****$P<0.0001$. **(f)** As in (e), except H1299^{WT} were transfected with siRNA against PRIM1 (siPRIM1) or control siRNA (siCtrl) 72

hr prior to PLA assay. Scale bar, 50μm. **(g)** Immunoblot analysis of H1299$^{RBM10\text{-}KO}$ cells expressing Flag-RBM10^{WT}, Flag-RBM10$^{\Delta RRM2}$, Flag-RBM10$^{\Delta ZNF1}$, or vector only (VO). Top: Representative immunoblot image using the indicated antibodies. α-Tubulin is used as a loading control. Bottom: Quantification of γH2AX band intensity (relative to H3) and pRPA32-S33 band intensity (relative to RPA32). Data are presented as mean ± s.d. (n=3). Statistical significance was determined by unpaired t-test. ***P<0.01;****P<0.0001;ns, not significant*. **(h,i)** Left: Representative immunofluorescence microscopy images of HDAC1:EdU-biotin (h) and H4K16ac:EdU-biotin (i) PLA in H1299^{WT} and H1299$^{RBM10\text{-}KO}$ cells. Cells were labelled with EdU for 20 min and were either left untreated (UT), treated with 1 mM HU for 1 h (HU). DAPI is used to stain nuclei. Scale bar, 20μm. Right: Quantification of PLA intensity per nucleus. Data are presented as mean PLA intensity per nucleus ± SEM (n>50). Statistical significance was determined by Mann-Whitney test. **P<0.05;**P<0.01;***P<0.001*. **(j)** Top: Representative immunofluorescence microscopy images of R-loops detected by S9.6 antibody in H1299^{WT} and H1299$^{RBM10\text{-}KO}$ cells. Cells overexpressing RNaseH1 are used as a negative control. DAPI is used to stain nuclei. Scale bar, 10μm. Bottom: Quantification of S9.6 signal in H1299^{WT} and H1299$^{RBM10\text{-}KO}$ cells. Data are presented as mean intensity per nucleus ± SEM (n>50 cells) and representative of 3 independent experiments. Statistical significance was determined by Mann-Whitney test. *****P<0.0001*.

The role of RBM10 in replication stress response is distinct from its splicing activity

Since RBM10 modulates the splicing of hundreds of genes, we sought to test whether the splicing activity of RBM10 underlies its role in the DNA replication stress response. To address this, we reintroduced RBM10-deficient cells with a vector expressing either flag-RBM10-WT or RBM10$^{\Delta ZNF1}$ or RBM10 mutant that lack RRM2 domain (RBM10$^{\Delta RRM2}$), known to modulate RBM10 splicing activity[60]. Subsequently, we assessed the ability of these RBM10 mutants to restore both splicing efficiency and the levels of replication stress markers to normal levels.

Our results demonstrate that while RBM10$^{\Delta ZNF1}$ successfully restores the splicing efficiency of RBM10 target genes, NUMB and EIF4H, it still exhibits increased levels of replication stress markers compared to cells expressing RBM10-WT (Fig. 3g and Supplementary Fig. 4c,d). Conversely, RBM10-deficient cells expressing RBM10$^{\Delta RRM2}$ mutant show defects in the splicing of RBM10 target genes but display normal levels of replication stress markers compared to control cells. These findings collectively support the notion that the role of RBM10 in DNA replication is independent of its splicing activity. To further validate this observation, we conducted transcriptome analysis of RBM10 in isogenic HCC827 and NCI-H1299 cells. Results revealed no discernible changes in the expression of core DNA replication and repair genes (Supplementary Fig. 4e and Supplementary Table 2). Our findings align with previously reported transcriptome analyses of RBM10 in various cell lines, demonstrating that RBM10 does not regulate the expression or splicing of core DNA replication and repair genes[6,32].

299

300 **RBM10 targets HDAC1 to active replication fork to fine-tune histone acetylation**

301 To elucidate the mechanistic role of RBM10 in DNA replication progression and replication
302 stress response, we focused on RBM10-HDAC1 interaction that has been identified in the
303 RBM10 interactome and validated through immunoprecipitation (Fig. 3b and Supplementary
304 Fig. 3b). Also, fission yeast Rbm10 was previously shown to interact with Clr6, a homolog of
305 human HDAC1/2[36]. In addition, previous reports have shown that HDAC1 is localized at active
306 DNA replication forks, where it deacetylates histones to prevent replication fork collapse[62–65].
307 Prompted by this, we sought to investigate whether RBM10 is essential for recruiting HDAC1
308 to DNA replication forks. Our results demonstrated a pronounced disruption in the association
309 of HDAC1 with DNA replication in RBM10-deficient cells under normal and stress conditions
310 (Fig. 3h). Consequently, the levels of H4K16 acetylation were increased in RBM10-deficient
311 cells compared to control cells (Fig. 3i). In summary, these data suggest that RBM10 serves as
312 an anchor for recruiting HDAC1 to active replication forks to facilitate the deacetylation of
313 H4K16, a modification recently recognized as crucial for replication fork stability[65,66]. Since a
314 recent work demonstrated that histone deacetylation counteracts the levels of R-loops at active
315 replication forks to mitigate transcription-induced replication stress[66], we postulated that the
316 increased levels of H4K16ac in RBM10-deficient cells is also accompanied by increased R-
317 loops levels. Indeed, we observed that RBM10-deficient cells exhibit elevated levels of R-loops
318 in S-phase cells, indicating that replication stress observed upon RBM10 loss is mediated, at
319 least in part, by transcription-replication conflicts and R-loop accumulation (Fig. 3j and
320 Supplementary Fig. 4f,g).

321 Additionally, since RBM10 interacts with RAD51 protein (Figure 3b) which has a central role
322 in homology repair (HR) of double-strand breaks (DSB) and its depletion impairs HR repair
323 leading to replication stress[67,68], we sought to investigate the functional relevance of their
324 interaction[67,68]. We aimed to determine whether the replication stress in RBM10-deficient cells
325 is due to defective HR repair. Toward this, we assessed the efficacy of HR repair of DSBs
326 using the Cas9-mClover-LMNA assay[69]. Results indicate that RBM10 deficiency has no
327 discernible effect on the percentage of mClover-positive cells (representing cells that repaired
328 DSBs through HR) compared to control cells (Supplementary Fig. 4h). This observation
329 suggests that the replication stress observed in RBM10-deficient cells is not attributed to
330 defective HR repair. This data raises an interesting possibility that the RBM10-RAD51
331 interaction might be required for replication fork reversal rather than HR repair.

332

333 **WEE1 kinase inhibition selectively sensitizes RBM10-deficient LUAD cells**

334 Herein, we sought to exploit the role of RBM10 in replication stress to selectively target
335 RBM10-deficient LUAD cells. Towards this, we focused on WEE1 kinase, since it is a high
336 scoring RBM10 SL gene that was identified in the three scoring methods (BAGEL, MAGeCK
337 and CCA) (Fig. 1b and Supplementary Fig. 1e,f), and is involved in several RBM10 SL
338 pathways, such as S-phase and G2/M cell cycle checkpoints, and was shown to protect the
339 stability of stalled replication forks[70–72]. Moreover, WEE1 has a small molecule inhibitor,
340 MK1775 (AZD1775), which is currently in several phase II clinical trials for treatment of
341 advanced solid tumors (ClinicalTrials.gov), highlighting the clinical potential of targeting
342 RBM10-deficient LUAD[73–75]. To test whether the observed RBM10-WEE1 synthetic lethality
343 (Fig. 1e) is dependent on WEE1 kinase activity, we pharmacologically inhibited WEE1 using
344 MK1775 in parental HCC827-Cas9^{WT} and two HCC827-Cas9$^{RBM10\text{-}KO}$ cell lines. Short and
345 long-term survival assays revealed that HCC827-Cas9$^{RBM10\text{-}KO}$ cells exhibit pronounced
346 sensitivity to MK1775 treatment compared to parental cells (Fig. 4a,b, Supplementary Fig. 5a).
347 The hypersensitivity of RBM10-deficient cells to MK1775 was also observed in RBM10-KO
348 (KO3) cells derived from naïve HCC827 cells that do not stably express Cas9, suggesting that
349 RBM10-WEE1 synthetic lethality is not due to a clonal effect or cytotoxicity caused by stable
350 expression of Cas9 endonuclease (Supplementary Fig. 5b,c). In addition, complementing
351 RBM10-deficient cells with a vector expressing flag-RBM10-WT suppressed the sensitivity to
352 MK1775 compared to cells expressing empty vector (Fig. 4c).

353 Similar to p53-proficient HCC827, our results showed that H1299$^{RBM10\text{-}KO}$ cells are
354 hypersensitive to MK1775 compared to control cells (Fig. 4d,e). To increase the therapeutic
355 potential of our observations, we tested RBM10-WEE1 synthetic lethality in two RBM10-
356 deficient patient-derived cell lines, NCI-H1944 (containing KRAS^{G13D} mutation) and NCI-
357 H1975 (containing EGFR$^{L858R/T790M}$ mutation) harboring p.A683Rfs*10 and p.G905Afs*7
358 truncating RBM10 mutations, respectively. Towards this, NCI-H1944 and NCI-H1975 cells
359 were transduced with flag-RBM10 expression vectors (Supplementary Fig. 5d,e) and treated
360 with MK1775 followed by cell viability assays. Results showed that RBM10 expression
361 rescues the sensitivity of RBM10-deficient cell lines to MK1775, suggesting that RBM10 loss
362 occurring during LUAD tumorigenesis potentiates the sensitivity to WEE1 inhibition (Fig.
363 4f,g). Altogether, our results recapitulate RBM10-WEE1 synthetic lethality observed in our
364 CRISPR-Cas9 SL screen and demonstrate that WEE1 inhibition selectively sensitizes RBM10-

deficient LUAD tumor cells from different origins and independently of common co-occurring mutations such as EGFR, KRAS and TP53, highlighting the clinical relevance of targeting

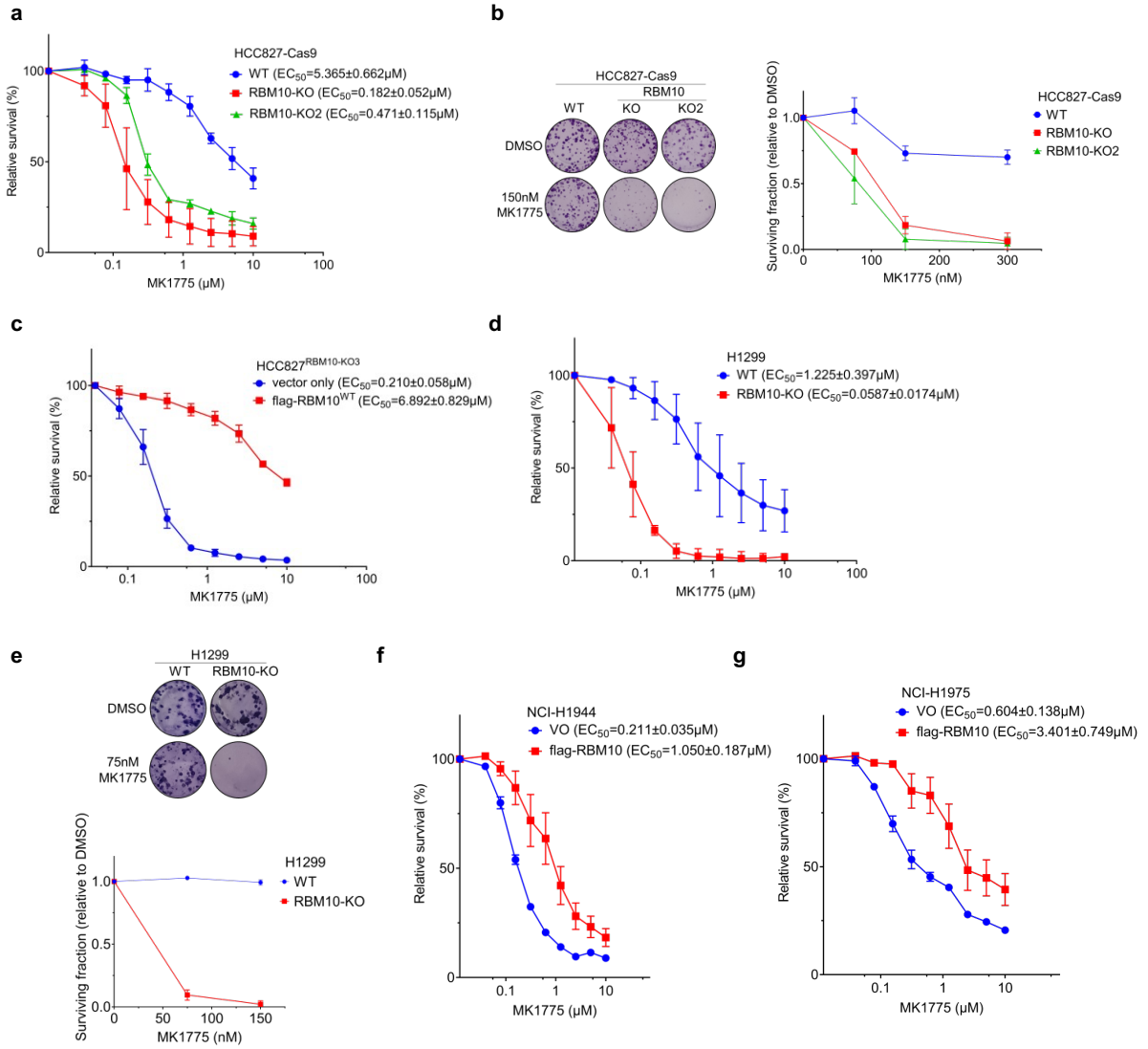

RBM10 loss in LUAD using MK1775.

Figure 4: WEE1 kinase inhibition selectively sensitizes RBM10-deficient LUAD cells. (a) Short-term cell viability assay and EC_{50} determination in WT and two RBM10-KO clones (KO and KO2) of HCC827-Cas9 cells treated with increasing concentrations of MK1775. Data are presented as mean ± s.d. (n=3). **(b)** Clonogenic survival of WT and two RBM10-KO clones treated with the indicated concentrations of MK1775. Left, representative images of plates stained with crystal violet. Right, quantification of clonogenic survival. Data are presented as mean ± s.d. (n=3). **(c)** As in (a), except of using $HCC827^{RBM10\text{-}KO3}$ cells expressing flag-RBM10-WT or vector only. (**d**) As in (a), except of using $H1299^{WT}$ and $H1299^{RBM10\text{-}KO}$ cells. **(e)** Clonogenic survival of $H1299^{WT}$ and $H1299^{RBM10\text{-}KO}$ cells treated with the indicated concentrations of MK1775. Top: Representative images of plates stained with crystal violet. Bottom: Quantification of clonogenic survival. Data are presented as mean ± s.d. (n=3). **(f,g)** As in (a), except of using NCI-H1944 (f) or NCI-H1975 (g) cells expressing either flag-RBM10-WT or vector only.

382

383 **DNA damage and premature mitotic entry underpin RBM10-WEE1 synthetic lethality**

384 We sought to decipher the molecular basis underlying the hypersensitivity of RBM10-deficient
385 cells to WEE1 inhibition. We showed that H1299$^{RBM10-KO}$ cells treated with increasing
386 concentrations of MK1775 exhibit elevated levels of phosphorylated histone H2A.X (γH2AX),
387 suggesting that DNA damage accumulation upon WEE1 inhibition is exacerbated in RBM10-
388 deficient cells (Fig. 5a). Likewise, higher levels of stalled forks and replication stress markers
389 including phosphorylated RPA32 on positions 4 and 8 (pRPA32-S4/S8), RPA32 on position
390 33 (pRPA32-S33), and CHK1 on position 345 (pCHK1-S345) were observed in MK1775-
391 treated H1299$^{RBM10-KO}$ cells compared to control cells (Fig. 5b and Supplementary Fig 6a,b).
392 Since WEE1 inhibition in RBM10-deficient cells leads to excessive replication stress, we
393 investigated the effect of MK1775 treatment on replication fork progression. Results showed
394 that WEE1 inhibition exacerbates the decrease in replication fork rate in RBM10-deficient cells
395 compared to parental cells (Supplementary Fig. 6c). To determine whether the increase in
396 replication stress following WEE1 inhibition was due to an increase in DNA breakage, we used
397 alkaline and neutral comet assays to measure the single-stranded DNA (ssDNA) breaks and
398 double-stranded DNA (dsDNA) breaks, respectively. Results show that MK1775 treatment in
399 RBM10-KO cells led to increased accumulation of both ssDNA and dsDNA breaks, with the
400 increase in ssDNA breaks being more prominent (Fig. 5c,d and Supplementary Fig. 6d). Next,
401 we utilized native BrdU staining to further confirm the increase in ssDNA in H1299$^{RBM10-KO}$
402 cells upon MK1775 treatment (Fig. 5e,f). To address whether the accumulation of ssDNA upon
403 WEE1 inhibition is due to ssDNA gaps arising during DNA replication, we used a modified
404 DNA combing assay incorporating a digestion step with S1 nuclease[76]. Results revealed that
405 labelled DNA tracks in MK1775-treated RBM10-KO cells showed high sensitivity to S1
406 nuclease digestion compared to MK1775-treated parental cells, suggesting WEE1 inhibition in
407 RBM10-KO cells leads to accumulated ssDNA gaps during DNA replication (Fig 5g).
408 Altogether, our results suggest that WEE1 inhibition exacerbates replication stress upon
409 RBM10 loss and that replication stress underpins, at least partly, RBM10-WEE1 synthetic
410 lethality.

411 Next, we sought to determine the effect of WEE1 inhibition on cell cycle progression in
412 RBM10-deficient cells. Towards this, parental and H1299$^{RBM10-KO}$ cells were co-stained for
413 pH3(Ser10), a marker of early mitosis, and EdU as a marker for S-phase following MK1775
414 treatment. Remarkably, unlike parental cells, a significant fraction (~45%) of MK1775-treated

H1299$^{RBM10\text{-}KO}$ cells were co-stained with EdU and pH3(Ser10), suggesting that WEE1 inhibition leads to premature mitotic entry in RBM10-deficient cells (Fig. 5h,i). Similar results were also obtained in parental and HCC827$^{RBM10\text{-}KO}$ cells (Fig. 5j). Consequently, we observed that MK1775-treated H1299$^{RBM10\text{-}KO}$ cells exhibit high levels of micronucleation, extensive nuclear γH2AX staining and apoptosis (Fig. 5k,l and Supplementary Fig. 6e). Altogether, we concluded that the sensitivity of RBM10-deficient cells to MK1775 is mediated by increased replication stress and premature mitotic entry leading to mitotic catastrophe and cell death.

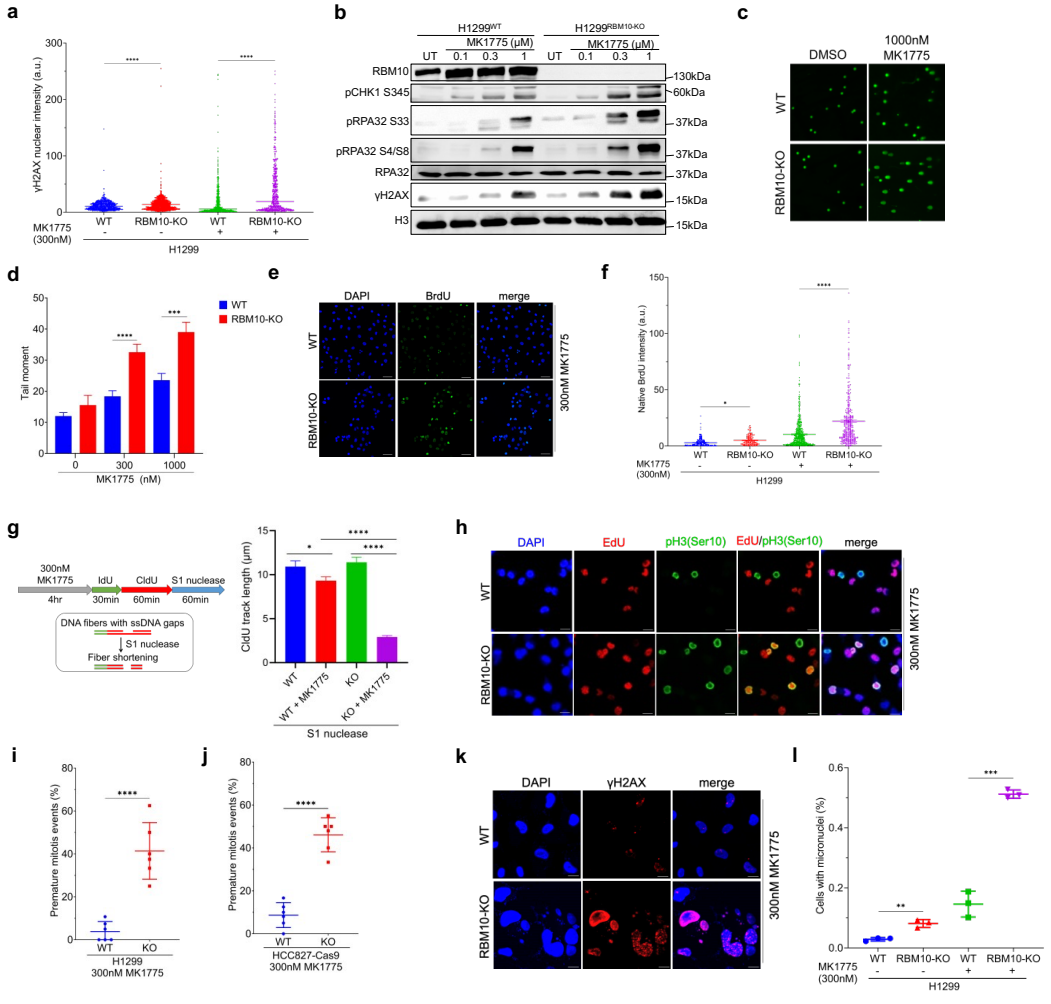

Figure 5: DNA damage and premature mitotic entry underpin RBM10-WEE1 synthetic lethality. (a) Quantification of γH2AX staining in H1299^{WT} and H1299$^{RBM10\text{-}KO}$ cells treated with 300nM MK1775 for 24 hr. Data are presented as mean nuclear intensity ± SEM (n>590 cells) and representative of 3 independent experiments. Statistical significance was determined by Mann-Whitney test. ****$P<0.0001$. **(b)** Immunoblot analysis of DNA damage and replication stress markers in H1299^{WT} and H1299$^{RBM10\text{-}KO}$ cells after MK1775 treatment. Cells were either left untreated (UT) or treated with the indicated concentrations of MK1775 for 24 hr followed by immunoblot analysis using the indicated antibodies. Histone H3 is used as a loading control. The positions of molecular weight markers are indicated to the right. **(c,d)** Alkaline comet assay in H1299^{WT} and H1299$^{RBM10\text{-}KO}$ cells treated either with DMSO or the

433 indicated concentrations of MK1775 for 24 hr. (c) Representative fluorescence microscopy
434 images of alkaline comet assay. (d) Quantification of DNA damage represented by comet tail
435 moment. Data are presented as mean tail moment ± SEM (n>150) and representative of 3
436 independent experiments. Statistical significance was determined by Mann-Whitney test.
437 ****P<0.001;****P<0.0001*. **(e,f)** Analysis of ssDNA levels using native BrdU staining in
438 H1299^{WT} and H1299$^{RBM10\text{-}KO}$ cells treated with 300nM MK1775 for 24 hr. (e) Representative
439 immunofluorescence microscopy image for native BrdU staining. DAPI is used to stain nuclei.
440 Scale bar, 50µm. (f) Quantification of native BrdU staining. Data are presented as mean nuclear
441 intensity ± SEM (n>100 cells for untreated cells, n>300 for MK1775-treated cells) and
442 representative of 3 independent experiments. Statistical significance was determined by Mann-
443 Whitney test. *****P<0.0001*. **(g)** H1299^{WT} and H1299$^{RBM10\text{-}KO}$ cells were either untreated or
444 treated with 300nM MK1775 for 4 hr followed by DNA combing analysis as indicated. The
445 length of CldU+ region of IdU+ CldU+ replication tracks was measured following digestion
446 with S1 nuclease for 1 hr. Data are presented as mean track length ± SEM (n>100). Statistical
447 significance was determined by Mann-Whitney test. **P<0.05;****P<0.0001*. **(h)**
448 Representative immunofluorescence microscopy images showing premature mitotic entry in
449 H1299^{WT} and H1299$^{RBM10\text{-}KO}$ cells treated with MK1775. EdU incorporation and pH3(Ser10)
450 were used to determine DNA synthesis and mitotic entry, respectively. DAPI is used to stain
451 nuclei. Scale bar, 20µm. **(i,j)** Quantification of premature mitotic entry events in parental (WT)
452 and H1299$^{RBM10\text{-}KO}$ (i) and HCC827$^{RBM10\text{-}KO}$ (j) cells. Premature mitosis events were calculated
453 as the percentage of EdU-positive cells from the pH3(Ser10)-positive (mitotic) cells and
454 presented as mean ± s.d. (n=6). Statistical significance was determined by unpaired t-test.
455 *****P< 0.0001*. **(k)** Representative immunofluorescence microscopy images of γH2AX and
456 DAPI staining in H1299^{WT} and H1299$^{RBM10\text{-}KO}$ cells treated with 300nM MK1775 for 24 hr.
457 Scale bar, 10µm. **(l)** Quantification of micronuclei in H1299^{WT} and H1299$^{RBM10\text{-}KO}$ cells treated
458 with 300nM MK1775 for 24 hr. Data are presented as the average percentage of cells with
459 micronuclei ± SEM (n=3). Statistical significance was determined by unpaired t-test.
460 *****P<0.0001.*
461

462 **MK1775 inhibits the growth of RBM10-deficient LUAD tumors *in vivo***

463 Given that the WEE1 inhibitor MK1775 is currently undergoing phase II clinical trials for
464 treating several tumor types[77], we sought to test the therapeutic potential of WEE1 inhibition
465 against RBM10-deficient LUAD cells *in vivo*. Our results showed that MK1775 treatment
466 prominently reduced the size of xenograft tumors derived from HCC827$^{RBM10\text{-}KO}$ and
467 H1299$^{RBM10\text{-}KO}$ cells, but not their parental counterparts (Fig. 6a,b and Supplementary Fig.
468 7a,b). Consistent with the observed γH2AX phenotype *in vitro*, RBM10-deficient tumors
469 exhibit increased levels of DNA damage in MK1775-treated mice (Fig. 6c,d and
470 Supplementary Fig. 7c).

471 Collectively, these findings strongly suggest that RBM10 loss leads to increased sensitivity to
472 WEE1 inhibition *in vivo*, independently of EGFR or TP53 status. To further substantiate the
473 clinical relevance of targeting RBM10-deficient LUAD, we tested the anti-tumor effect of
474 MK1775 against tumor xenografts derived from patient-derived LUAD cells, NCI-H1944 and

475 NCI-H1975, harboring naturally occurring RBM10 cancer mutations. Results showed that
476 WEE1 inhibition leads to remarkable tumor growth inhibition in RBM10-deficient NCI-H1975
477 and NCI-H1944 compared to RBM10-proficient cells (Fig. 6e). Altogether, our results

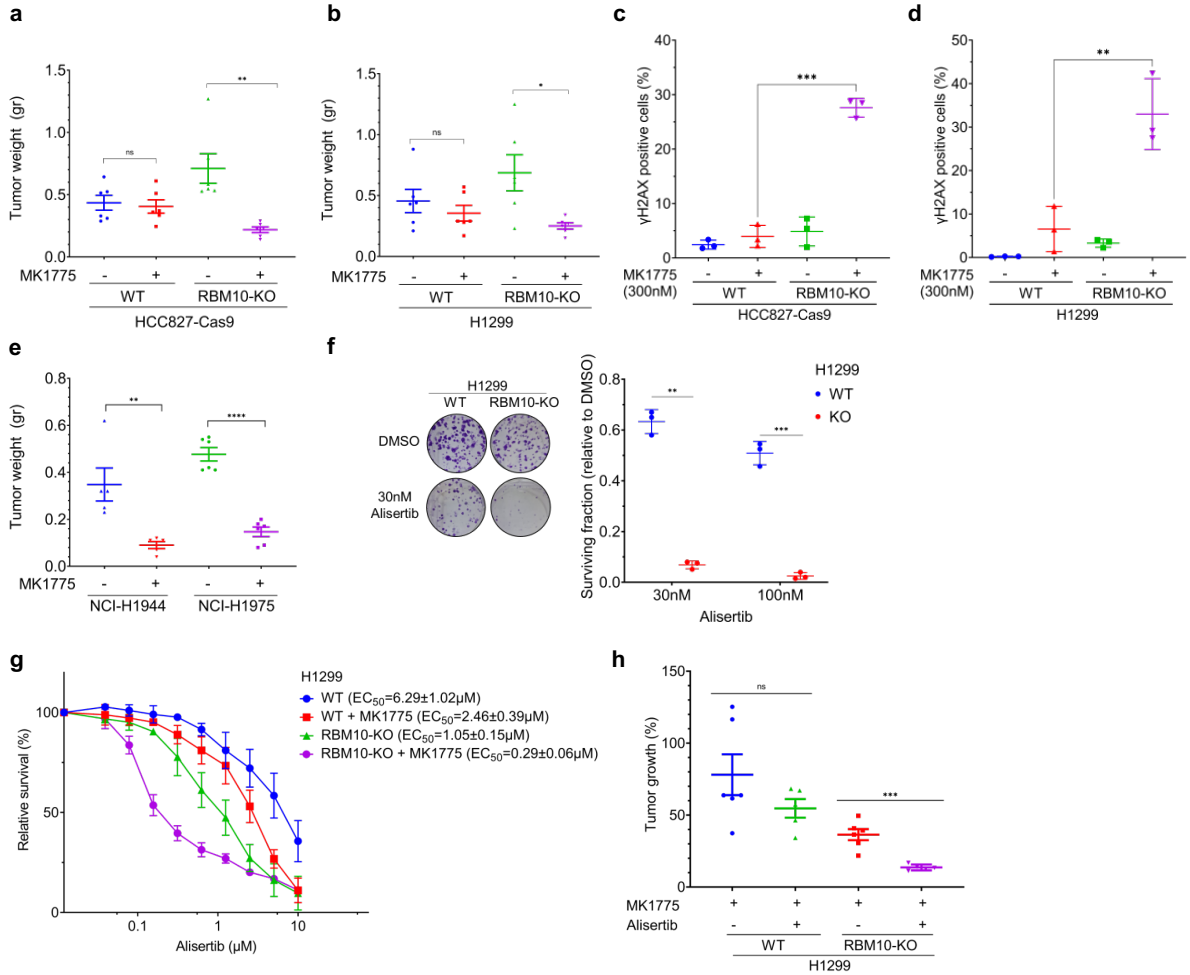

478 demonstrate the therapeutic efficacy of MK1775 as a single-agent in eradicating LUAD tumors
479 harboring RBM10 deleterious cancer mutations.

480 **Figure 6: MK1775 inhibits the growth of RBM10-deficient LUAD cells *in vivo*. (a,b)**
481 Tumor weight of parental (WT) and HCC827-Cas9$^{RBM10-KO}$ (a) and H1299$^{RBM10-KO}$ (b)
482 xenografts treated with either MK1775 or vehicle. MK1775 was administered once daily at
483 40mg/kg for 15 days. Results are shown as mean tumor weight ± SEM (n=6). Statistical
484 significance was determined by unpaired t-test. *$P<0.05$;**$P<0.01$. **(c,d)** Quantification of
485 γH2AX immunostaining in xenograft tumor sections from parental and HCC827-Cas9$^{RBM10-KO}$
486 (c) and H1299$^{RBM10-KO}$ (d) tumors treated with either MK1775 or vehicle. Data are presented
487 as the average percentage γH2AX positive cells ± SEM of 3 different tumor sections for each
488 group. Statistical significance was determined by unpaired t-test. **$P<0.01$;***$P<0.001$. **(e)**
489 Tumor weight of NCI-H1944 and NCI-H1975 xenografts treated with either MK1775 or
490 vehicle. MK1775 was administered once daily at 40mg/kg for 15 days. Results are shown as
491 mean tumor weight ± SEM (n=5 for NCI-H1944, n=6 for NCI-H1975). Statistical significance
492 was determined by unpaired t-test. **$P<0.01$;****$P<0.00001$. **(f)** Clonogenic survival of
493 H1299^{WT} and H1299$^{RBM10-KO}$ cells treated with the indicated concentrations of alisertib. Left,
494 representative images of plates stained with crystal violet. Right, quantification of clonogenic

495 survival. Data are presented as mean ± s.d. (n=3). **(g)** Short-term cell viability assay and EC_{50}
496 determination in $H1299^{WT}$ and $H1299^{RBM10\text{-}KO}$ cells treated with increasing concentrations of
497 alisertib with or without treatment with 300nM MK1775. Data are presented as mean ± s.d.
498 (n=3). **(h)** Tumor growth inhibition in $H1299^{WT}$ and $H1299^{RBM10\text{-}KO}$ xenografts treated with
499 MK1775 alone, MK1775 and alisertib combination, or vehicle. MK1775 alone or MK1775 and
500 alisertib combination were administered once daily at 30mg/kg for 15 days. Results are shown
501 as percentage tumor growth inhibition relative to vehicle ± SEM (n=6 for MK1775 alone and
502 vehicle, n=5 for MK1775 + alisertib combination). Statistical significance was determined by
503 unpaired t-test. ***$P<0.001$.

504

505 **Aurora kinase A inhibition exacerbates the anti-tumor activity of WEE1 inhibition in**
506 **RBM10-deficient LUAD**

507 Given that both WEE1 and Aurora A (AURKA) scored highly in RBM10 SL screen and both
508 kinases are targeted by small molecule inhibitors undergoing clinical trials, we tested the
509 efficacy of the combined Aurora A and WEE1 inhibition on the growth of RBM10-deficient
510 LUAD. First, we observed that the Aurora A inhibitor, alisertib, had a profound effect on the
511 clonogenic survival of RBM10 KO cells, concurrent with the CRISPR SL screen results (Fig.
512 6f and Supplementary Fig. 7d). Moreover, while alisertib alone led to a significant reduction
513 in RBM10-deficient cell viability, combined MK1775 and alisertib treatment further
514 exacerbated cell toxicity (Fig. 6g). Prompted by this, we tested the effect of the combined
515 MK1775 and alisertib treatment on the growth of RBM10-deficient xenograft tumors. Results
516 showed that the combined treatment leads to a profound and significant reduction in RBM10-
517 deficient tumor size that is greater than the reduction upon MK1775 treatment alone (Fig. 6h).
518 Therefore, we concluded that Aurora kinase A inhibition might be a viable therapeutic strategy
519 to enhance the anti-tumor activity of WEE1 inhibition in RBM10-deficient LUAD tumors.

520 **Discussion**

521 We present a model that underscores a new function of RBM10 in both DNA replication
522 progression and replication stress response (Fig. 7). RBM10 interactome analysis revealed that
523 it interacts with various replication fork components that are required for proper replication
524 fork progression, as well as recovery from replication stress. Also, we show that RBM10
525 depletion leads to replication fork slowdown, which is accompanied by an increase in DNA
526 damage. Our data are in line with a genome-wide siRNA screen that identified RNA processing
527 factors, including RBM10, as replication stress response genes[56]. Moreover, previous studies
528 showed that RBM10 is associated with human pre-replication complex[78] and interacts with
529 several proteins involved in DNA replication and repair in fission yeast[36]. In this regard, it
530 would be of interest to determine whether other RNA splicing and processing factors are also

531 implicated in DNA replication. In this study, we show that the RNA-binding protein RBM10
532 is recruited to active DNA replication forks in a PRIM1-dependent manner to fine-tune the
533 levels of histone acetylation at active DNA replication fork. Given that PRIM1 knockdown
534 alleviates RBM10 association with active replication forks, we propose a model that this
535 association requires RNA molecules, presumably the RNA primers of Okazaki fragments. In
536 this regard, we revealed that the RBM10 ZnF1 domain, known for its RNA-binding capability,
537 mediates its association with replication fork. Interestingly, this ZnF1 domain is found in
538 various proteins including MDM2, NEIL3, ZRANB3, and FUS that have been previously
539 implicated in regulating DNA replication progression and stress response[79–82]. Future
540 investigations will be necessary to determine whether the association of these proteins with
541 DNA replication forks is mediated by the RNA primers of Okazaki fragments. Functionally,
542 we demonstrate that RBM10 counteracts the formation of R-loops in S-phase cells,
543 concurrently facilitating the association of HDAC1 with active replication forks to deacetylate
544 H4K16. These findings align with recent studies that described a role of HDAC1/2 in chromatin
545 remodeling at active replication forks to maintain normal replication fork progression and
546 replication fork stability[64–66]. Interestingly, it was shown that HDAC1/2 decrease the levels of
547 the transcriptionally active H4K16 acetylation at replication forks, thereby reducing the levels
548 of R-loops and mitigating transcription-induced replication stress[66]. Further work will be
549 required to determine the impact of RBM10 depletion on the acetylation levels of other histone
550 and non-histone residues that are implicated in DNA replication regulation. While our data
551 suggest that RBM10 function in DNA replication is distinct from its splicing activity (Fig. 3g),
552 we cannot exclude the possibility that RBM10 may regulate the splicing or expression of genes
553 involved in regulating replication fork progression.

554 In this study, we performed a genome-wide CRISPR-Cas9 knockout screen employing
555 isogenic LUAD cells carrying RBM10 cancer mutation, a type of nonsense mutation occurring
556 with frequencies ranging from 9% to 25% in LUAD. We identified ~250 RBM10 SL genes,
557 such as WEE1 and Aurora A kinases, which can be therapeutically exploited for eradicating
558 RBM10-deficient LUAD tumors. Indeed, pharmacological inhibition of WEE1 using MK1775
559 markedly reduces RBM10-deficient cell proliferation and tumor growth. Given that MK1775
560 is currently in phase II clinical trials for the treatment of several types of tumors, we propose
561 that it can be also used against RBM10-deficient LUAD with immediate clinical applicability.
562 Interestingly, the sensitivity of RBM10-deficient cells to WEE1 inhibition is further
563 exacerbated by the combined treatment with alisertib, an Aurora Kinase A inhibitor. This

564 synergistic effect between these two inhibitors is in agreement with a previous study showing
565 that simultaneous inhibition of Aurora A and WEE1 prompts cells to traverse the G2–M
566 checkpoint in the presence of DNA damage and impaired spindle assembly, culminating in
567 mitotic catastrophe. Consequently, it leads to a synergic anti-tumor effect in p53-deficient
568 squamous cell carcinoma of the head and neck[83]. Together, these observations provide a basis
569 for testing this combination for clinical treatment of RBM10-deficient LUAD patients, thus
570 increasing therapeutic benefits and minimizing the risk for developing resistance.

571 Mechanistically, RBM10-WEE1 synthetic lethality is mediated, at least in part, by increased
572 replication stress leading to premature mitotic entry and cell death. This finding supports the
573 notion that the sensitivity of RBM10-deficient cells to WEE1 inhibition is dependent on the
574 emerging role of RBM10 in DNA replication. Our data are therefore in agreement with
575 previous studies showing synergistic interaction between WEE1 inhibition and replication
576 stress-inducing agents[84–87].

577 Intriguingly, a previous report showed that RBM10 deficiency in LUAD is associated with
578 enriched immune pathways, elevated tumor mutational burden, and increased human leukocyte
579 antigens (HLA) expression, suggesting that RBM10 deficiency may enhance anti-tumor
580 immunity in LUAD[88]. In agreement with this, our RBM10 transcriptome in HCC827 and
581 H1299 cell lines showed that RBM10 depletion leads to increased expression of
582 proinflammatory cytokines such as IL1R2, TNFRSF1B, BMP2, IL7R and CCL2. Further work
583 will be vital to determine whether WEE1 inhibition in RBM10-deficient tumors further
584 amplifies the upregulation of genes associated with immune pathways, which might enhance
585 the response to immune therapies.

586 Unbiased genome-wide CRISPR-Cas9 SL screens revolutionized the discovery of novel SL
587 interactions that can be exploited for developing new cancer therapies[89,90]. Our CRISPR-Cas9
588 knockout screen revealed ~250 RBM10 SL genes involved in various cellular pathways, such
589 as RNA splicing and cell cycle. These genetic interactions advance our understanding of the
590 physiological functions of RBM10 and provide a repertoire of novel targets that can be
591 harnessed to formulate new strategies for targeting RBM10-deficiency. Interestingly, RBM10
592 is frequently mutated in various human cancers such as endometrial (8%) and urothelial (5%)
593 carcinomas[58]. Therefore, our findings might be of clinical interest to other types of human
594 cancer harboring RBM10 mutations.

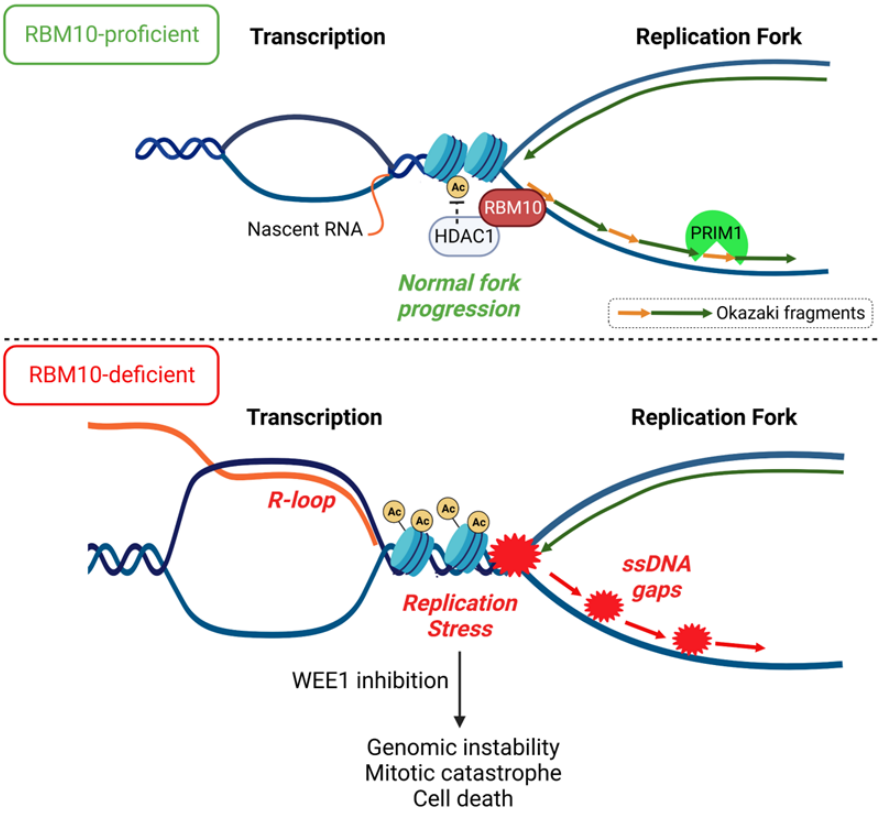

Figure 7: Model depicting the novel role of RBM10 in DNA replication and replication stress response. (Top) RBM10 association with active DNA replication forks is dependent on PRIM1, which synthetizes the RNA primer of Okazaki fragments. RBM10 promotes the recruitment of HDAC1 to ongoing and stressed replication forks and ensures the deacetylation of H4K16, thereby limiting R-loop formation and maintaining fork stability. (Bottom) In RBM10-deficient cells, defective HDAC1 recruitment and H4K16 deacetylation at stressed replication forks contributes to R-loop accumulation, fork destabilization, and ssDNA gap formation leading to replication stress. High levels of replication stress render RBM10-deficient tumor cells sensitive to WEE1 kinase inhibition, leading to the accumulation of DNA damage and mitotic catastrophe resulting in tumor cell death. Created with BioRender.com.

Acknowledgments

We thank Avigail Yampolsky and Yarin Attar for helping in validating the RBM10 CRISPR-Cas9 screen results, Dvir Aran for his help in analyzing RBM10 mutations in cancer, Yossi Shiloh and Yehuda Assaraf for their insightful comments on the project. We also thank Nadav Sharon, Assaf Bester, and Juan Valcárcel for generously sharing reagents and plasmids. We thank Janette Zavin for histological processing. We thank our lab members for critical reading of the manuscript. We thank bioRENDER (biorender.com) for assisting in drawing the model and the schematics presented in the figures. Research in the Ayoub lab is supported by grants from the Israel Science Foundation (2511/19) and Israel Cancer Research Fund (22-110-PG). Research in the Simon lab is supported by grants from the Israel Science Foundation (1283/21) and the Binational Science Foundation (2019688 and 2021085). F.E.M. and E.R.A. are supported by Clore fellowship. A.B. is supported by Joan and Irwin Jacobs fellowship. N.A. is supported by the Neubauer Family foundation.

Author Contributions

F.E.M. wrote the original draft and performed all the experiments and analysis described in this manuscript except the ones indicated below. E.R.A. cloned flag-MCM5 expression plasmid and helped in setting up the CRISPR-Cas9 screen and proofreading the manuscript. J.K. performed the experiments described in Figure 2a, 2b, 5g and Supplementary Figure 2e, 5c. A.B. performed the experiments described in Supplementary Figure 2d, 3d and helped in characterizing RBM10 splicing activity. I.S. helped in analyzing the data related to RBM10 role in DNA replication progression and editing the manuscript. N.A. conceived and supervised the study.

Corresponding Author

Correspondence to Nabieh Ayoub (ayoubn@technion.ac.il).

Competing Interests

The authors declare that they have no competing interest.

649 **Methods**

650 **Cell lines and cell culture**

651 HCC827, NCI-H1299, NCI-H1944, and NCI-H1975 cell lines were obtained from ATCC and
652 grown at 37°C and 5% CO2 and cultured in RPMI-1640 medium (Gibco) supplemented with
653 10% heat-inactivated fetal bovine serum (Gibco), 2mM L-glutamine (Gibco), and 100unit/mL
654 penicillin and 100µg/mL streptomycin (Gibco). HEK293T cell line was obtained from ATCC
655 and grown at 37°C and 5% CO2 and cultured in Dulbecco's Modified Eagle Medium (DMEM)
656 (Gibco) supplemented with 10% heat-inactivated fetal bovine serum (Gibco), 2mM L-
657 glutamine (Gibco), and 100unit/mL penicillin and 100µg/mL streptomycin (Gibco).

658 **Lentiviral transduction**

659 Lentiviral particles were generated by co-transfecting HEK293T cells plated in 10cm plates
660 with 1.64pmol target vector, together with 1.3pmol psPAX2 (Addgene #12260) and 0.72pmol
661 pMD2.G (Addgene #12259) using 3:1 µg PEI to µg DNA ratio. Media containing the viral
662 particles were collected 48 hr post-transfection and filtered with 0.45 µm filters. The indicated
663 cell lines were transduced with the lentiviral particles in the presence of 10µg/ml polybrene
664 (Sigma-Aldrich H9268). At 48 hr post-infection, transduced cells were selected using the
665 appropriate antibiotics.

666 **Generation of Flag-Cas9 expressing cells and RBM10 knockout cell lines**

667 To generate HCC827 cell line constitutively expressing Cas9, cells were transduced with Lenti-
668 Cas9-2A-Blast (Addgene #73310) lentiviral particles followed by selection with 10µg/ml
669 blasticidin (Invivogen #ant-bl) for 72 hr. A single clone stably expressing Flag-Cas9 fusion
670 was selected and validated by western blot and immunofluorescence. To generate isogenic
671 RBM10 knockout in HCC827 cells expressing flag-Cas9 (HCC827-Cas9), guide RNAs
672 (gRNA) were designed and cloned into pSPgRNA plasmid (Addgene #47108) using BbsI
673 restriction enzyme. HCC827-Cas9 cells were transfected with RBM10 gRNA1 (HCC827-
674 Cas9$^{RBM10\text{-}KO}$ and naïve HCC827$^{RBM10\text{-}KO3}$) or gRNA2 (HCC827-Cas9$^{RBM10\text{-}KO2}$) followed by
675 clonal isolation. Single clones were screened for RBM10 knockout using western blot and
676 validated by immunofluorescence and sequencing. The sequences of RBM10 gRNAs are
677 included in Supplementary Table 3. To generate RBM10 knockout in naïve HCC827 and NCI-
678 H1299 cells, RBM10 gRNA1 was cloned into pSpCas9(BB)-2A-GFP (PX458) (Addgene
679 #48138) and transfected to cells. At 24 hr after transfection, GFP-positive cells were sorted
680 using BD LSRFortessa™ cell analyzer (BD Biosciences) and plated in 96-well plates at a

681 dilution of one cell per well. Single clones were screened for RBM10 knockout using western
682 blot and validated by immunofluorescence and sequencing.

683 **Genome-wide CRISPR-Cas9 synthetic lethal screen**

684 240 million cells of HCC827-Cas9^{WT} and HCC827-Cas9$^{RBM10\text{-}KO}$ were transduced in triplicates
685 with TKOv1 sgRNA library, which contains 91,320 sgRNAs targeting 17,232 protein-coding
686 genes[52], at MOI=0.3 and an average of 500-fold coverage of the library. 24 hr post-
687 transduction, cells were selected with 2 μg/mL puromycin for 2 days. Following selection, 80
688 × 10^7 cells were harvested as day 0 samples (T0) and the remaining cells were plated and
689 passaged every 5 days. Cells were then collected at day 15 (T15) for isolation of genomic DNA
690 (gDNA) together with the T0 samples. Genomic DNA extraction was performed with Blood
691 & Cell Culture DNA Maxi Kit (Qiagen) according to the manufacturer's instructions. gRNA
692 inserts were amplified using two rounds of PCR reactions. First, a 600bp region of the lentiviral
693 library vectors containing the sgRNA region was amplified using ordinary PCR with Q5 high-
694 fidelity DNA polymerase for 25 cycles. A total of 120μg gDNA was used as template for each
695 sample (60 reactions: 2μg gDNA/50μl reaction). Second, the amplified PCR products were
696 subjected to another PCR reaction with Illumina next-generation sequencing adaptors for 10
697 cycles and 200bp product was amplified. The resulting amplicons were pooled and gel purified
698 using the NucleoSpin Gel and PCR Clean-up (Macherey-Nagel). Samples were sequenced on
699 a MiSeq platform with ~10 million reads per sample (Illumina). Demultiplexing and mapping
700 of sequencing reads to the gRNA library was performed using MAGeCK[54]. Fold-change for
701 each gRNA was calculated in each replicate versus the T0 sample. 3 analysis methods were
702 used to predict RBM10 synthetic lethal genes: (1) Bioinformatic and Bayesian Analysis of
703 Gene Essentiality (BAGEL) algorithm[53] was devised to calculate the essentiality score (Bayes
704 factor – BF) of each gene in parental (WT) and RBM10-KO cells. RBM10 SL genes were
705 defined as genes with BF>5 (i.e. essential) in RBM10-KO cells and BF<2 (i.e. non-essential)
706 in WT cells. (2) CRISPR Counts Analysis (CCA)[55] was used to calculate synthetic lethality
707 score for each gene and genes with score > 0.8 were considered candidate RBM10 SL genes.
708 (3) MAGeCK was used to calculate log fold-change (LFC) for each gene and genes with LFC<-
709 1 in RBM10-KO cells with LFC difference > 1 between WT and RBM10-KO were considered
710 RBM10 SL genes. Pathway enrichment analysis and gene ontology were conducted using
711 ShinyGO[91]. STRING interaction network was performed using string-db.org.

712 **Conditional short hairpin RNA (shRNA) knockdown**

713 shRNA oligonucleotides directed against the indicated genes were annealed and cloned into
714 Tet-pLKO-puro lentiviral vector (Addgene #21915) digested with *Eco*RI and *Age*I. Lentiviral
715 particles were generated as described above and used to transduce parental and RBM10-KO
716 HCC827-Cas9 cells, followed by selection with 1μg/ml puromycin (Invivogen #ant-pr) for 3
717 days. Cells were maintained in complete medium in the presence of 0.6μg/ml puromycin. To
718 induce shRNA-mediated gene expression knockdown, cells were cultured in the presence of
719 0.2μg/ml doxycycline (DOX) for 48 hr prior to clonogenic survival assays. Gene expression
720 knockdown was validated by RT-qPCR. The shRNA and qPCR primer sequences used in this
721 study are included in Supplementary Table 4.

722 **Generation of expression vectors**

723 To generate EGFP-RBM10 expression vectors, RBM10 was amplified from pDest26-RBM10-
724 wt plasmid[32] (gift from Prof. Juan Valcárcel) and cloned into pEGFP-C1 expression plasmid.
725 To generate RBM10 deletion mutants, all-round PCR was used to delete the relevant regions.
726 To constitutively restore RBM10 expression in RBM10-deficient cells, full-length RBM10 and
727 RBM10 deletion mutants were subcloned to Lenti-Cas9-2A-Blast plasmid followed by
728 lentivirus generation and transduction. To generate Flag-MCM5 expression vector, MCM5 was
729 cloned from cDNA into p3X-Flag-CMV10 expression vector. Primer sequences used for
730 cloning and mutagenesis are included in Supplementary Table 4.

731 **Transfections**

732 Cell transfections with plasmid DNA or siRNA were performed using Polyethylenimine (PEI)
733 and Lipofectamine RNAiMax, respectively, following the manufacturer's instructions. siRNAs
734 used in this study are: RBM10 siRNA #1 (ThermoFisher Scientific HSS112075, 5′-
735 CAAACGCCGAGAGAAGUGCU-3′); RBM10 siRNA #2 (ThermoFisher Scientific
736 HSS112075, 5’-TTTGCCAAGGGTTCTAAGAG-3’); PRIM1 siRNA (Euphera Biotech
737 EHU105881); Stealth RNAi negative control (Invitrogen).

738 **RNA isolation, RT-PCR and qPCR**

739 Total RNA was isolated from cells using the TRIzol reagent according to the manufacturer's
740 instructions (Ambion) and treated with RQ1 DNase (M6101, Promega). 1μg RNA was used
741 for cDNA synthesis using the qScript cDNA Synthesis Kit (Quanta) with random primers. RT-
742 PCR for alternative splicing assay of NUMB and EIF4H genes was performed by standard
743 PCR using Red Load Taq Master (Jena Bioscience) followed by gel electrophoresis in agarose
744 gel stained with ethidium bromide. Band intensities were quantified using GelDoc software.
745 Real-time qPCR for measuring mRNA levels was performed using Step-One-Plus real-time

746 PCR System (Applied Biosystems) and the Fast SYBR Green Master mix (Applied
747 Biosystems) with three technical repeats for each PCR. Data analysis and quantification were
748 performed using StepOne software V2.2 supplied by Applied Biosystems. Primer sequences
749 used for RT-PCR and qPCR are included in Supplementary Table 4.

750 **Small molecule inhibitors and drugs**

751 MK1775 (A5755), Alisertib (MLN8237) (A4110), and hydroxyurea (B2102) were purchased
752 from APExBio. Caffeine was purchased from Sigma-Aldrich (C8961).

753 **Immunoblotting**

754 Whole-cell protein extracts were prepared using hot lysis buffer (1%SDS, 5mM EDTA, 50mM
755 Tris, pH7.5) supplemented with protease inhibitor mixture (Calbiochem). Protein samples were
756 diluted and boiled in 5X protein loading buffer (10% SDS, 500mM DTT, 50%Glycerol,
757 250mM Tris-HCL and 0.5%bromophenol blue dye) and separated on an SDS-polyacrylamide
758 gel. Proteins were transferred to a PVDF membrane (Millipore) and immunoblotted with the
759 indicated antibodies. The following primary antibodies were used for immunoblotting: RBM10
760 (Sigma-Aldrich cat.no. HPA034972, 1:10,000), FLAG-tag (Sigma-Aldrich cat.no. F7425,
761 1:4,000), β-actin (Sigma-Aldrich cat.no. A5441, 1:10,000), α-Tubulin (Santa Cruz Bio cat.no.
762 sc-5286, 1:1,000), pRPA32-S4/S8 (Bethyl cat.no. A300-245A, 1:1,000), pRPA32-S33 (Bethyl
763 cat.no. A300-246A, 1:1,000), RPA32 (Abcam cat.no. ab2175, 1:500), γH2AX (Cell Signaling
764 Technology cat.no. 2577, 1:1000), pChk1-S345 (Cell Signaling Technology cat.no. 2348,
765 1:1,000), Histone H3 (Abcam cat.no. ab1791, 1:30,000), Rad51 (Santa Cruz Bio cat.no. sc-
766 8349, 1:1,000), PARP1 (Enzo Life Sciences cat. no. ALX-210-895, 1:2,000), HDAC1
767 (GeneTex cat. no. GTX100513, 1:2,000), PCNA (Santa Cruz Bio cat. no. sc-56, 1:1,000),
768 GAPDH (Abcam cat.no. ab8245, 1:1,000), GFP (Santa Cruz Bio cat.no. sc-9996, 1:1,000). The
769 following secondary antibodies were used: anti-rabbit IgG-HRP (Jackson ImmunoResearch
770 cat.no. 111–035-003, 1:20,000), anti-mouse IgG-HRP (Amersham cat.no. NXA931, 1:10,000).
771 Immunoblot intensity quantification was performed using ImageJ.

772 **Biochemical fractionation**

773 Cells were lysed with Buffer A for 5 min at 4°C. Cell lysates were centrifuged at 1500× g for
774 5 min at 4°C and the supernatant (cytoplasmic fraction) was removed. Then, the pellet was
775 incubated with Buffer B (3mM EDTA, 0.2mM EGTA, 1mM DTT, PMSF, and protease
776 inhibitor mixture) for 10 min on ice followed by centrifugation at 1700× g for 5 min at 4°C to
777 extract nuclear-soluble fraction. To prepare chromatin-bound fraction, pellet was resuspended
778 with hot lysis buffer (1%SDS, 5mM EDTA, 50mM Tris, pH7.5), boiled for 15 min, and

779 sonicated with two 15 sec pulses of 35% amplitude, centrifuged at maximum speed for 20 min
780 at 12°C, and the supernatant was recovered. Fractions were subjected to immunoblot analysis
781 with the indicated antiabodies. For chromatin-bound fractionation with RNaseA, pellet was
782 first resuspended in Buffer A containing 5 µg RNase A and incubated for 2 hr at room
783 temperature followed by extraction with hot lysis buffer.

784 **GFP-trap**

785 HEK293T cells expressing either EGFP only or EGFP-RBM10 plasmids were subjected to
786 GFP-TRAP assay as previously described[92]. Where indicated, cells were also co-transfected
787 with Flag-MCM5 plasmid. Briefly, EGFP-RBM10 or EGFP-only expressing cells were lysed
788 in RIPA buffer (150mM NaCl, 50mM Tris pH 7.4, 1% NP40, 0.5% deoxycholate, 0.1% SDS)
789 supplemented with protease inhibitor cocktail and then diluted 1:4 with binding buffer (150mM
790 NaCl, 50mM Tris pH 7.4). 2 milligram of cell lysate was incubated for 4 hr at 4ºC with 15µl
791 GFP-TRAP beads followed by western blot analysis. For GFP-trap followed by mass
792 spectrometry (MS), HEK293T cells were transfected with EGFP-RBM10, lysed and subjected
793 to GFP-trap as described above. Beads were washed 5 times in PBSx1 followed by elution and
794 trypsin digestion. Digested peptides were then analyzed by mass spectrometry (MS) at the
795 Smoler Proteomics Center in the department of Biology in the Technion. The samples were
796 analyzed by LC-MS/MS using Q-Exactive plus mass spectrometer (Thermo Scientific),
797 coupled to Easy nano LC-1000 capillary UHPLC (Thermo Scientific). Protein identification
798 and intensity analysis was performed using maxquant[93], searching against the human section
799 of the Uniprot database. RBM10-interacting proteins enrichment analysis and gene ontology
800 was conducted using ShinyGO[91].

801 **Immunoprecipitation**

802 For endogenous RBM10 immunoprecipitation, H1299 cells were harvested and lysed in RIPA
803 buffer (150mM NaCl, 50mM Tris pH 7.4, 1% NP40, 0.5% deoxycholate, 0.1% SDS)
804 supplemented with protease inhibitor cocktail. Immunoprecipitations were performed using
805 0.5µg IgG or RBM10 antibody and protein A magnetic beads (GenScript #L00273) incubated
806 with 2mg lysate overnight at 4ºC. Immunoprecipitated samples were subjected to immunoblot
807 analysis using the indicated antibodies.

808 **Immunofluorescence**

809 Cells were seeded onto glass coverslips and grown for 24 hr followed by drug treatments as
810 indicated in the figure legends. Cells were fixed with 4% (wt/vol) paraformaldehyde for 10
811 min, permeabilized with 0.5% Triton X-100 in PBS for 10 min, blocked with blocking buffer

812 (4% (wt/vol) BSA, 0.15% Tween 20 and 0.15% Triton X-100 in PBS) for 1 hr at room
813 temperature and incubated with the indicated antibodies for 1 hr at 37°C. Excess antibody was
814 washed three times with wash buffer (0.15% Tween 20 and 0.15% Triton X-100 in PBS × 1),
815 and cells were stained with secondary antibodies for 1 hr at room temperature in the dark, and
816 then washed as above. Coverslips were mounted onto glass slides using VECTASHIELD®
817 Antifade Mounting Medium with DAPI (Vectorlabs). For immunofluorescence staining of
818 γH2AX, pRPA32-S33, and BrdU, cells were pre-extracted with 0.25% Triton X-100 in PBS
819 for 15 min on ice prior to fixation. For EdU incorporation, cells were pulsed with 10μM EdU
820 (5-ethynyl-2-deoxyuridine, Invitrogen A10044) for 30 min at 37ºC, 5% CO2. EdU click
821 reactions were performed after cell permeabilization by incubating cells with EdU staining
822 buffer containing 2mM CuSO4, 100mM ascorbic acid and 1μM AlexaFluor 647 azide
823 (Invitrogen A10277) in PBS for 30 min at room temperature. Images were acquired using
824 inverted Zeiss LSM-700 or LSM-710 confocal microscopes. Image analysis was performed
825 using ImageJ software. The following primary antibodies were used for immunofluorescence:
826 BrdU FITC (BD Biosciences, cat.no. 51-23614 1:1,000), RBM10 (Sigma-Aldrich cat.no.
827 HPA034972, 1:2,000), pRPA32-S33 (Bethyl cat.no. A300-246A, 1:500), γH2AX (Millipore
828 cat.no. 05-636, 1:2,500), FLAG-tag (Sigma-Aldrich cat.no. F7425, 1:1,000), pH3(Ser10) (Cell
829 Signaling Technology cat.no. 9706, 1:1,000), Anti-DNA-RNA Hybrid Antibody, clone S9.6
830 (Sigma-Aldritch cat.no. MABE1095, 1:1,000). The following secondary antibodies were used:
831 anti-rabbit IgG Alexa Fluor®488 (Invitrogen cat.no. A-21206, 1:500), anti-mouse IgG Alexa
832 Fluor®488 (Invitrogen cat.no. A-21202, 1:500), anti-rabbit Alexa Fluor®568 (Invitrogen cat.no.
833 A10042, 1:500), anti-mouse Alexa Fluor®568 (Invitrogen cat.no. A10037, 1:500), anti-rabbit
834 Alexa Fluor®647 (Invitrogen cat.no. A-31573, 1:500), anti-mouse IgG Alexa Fluor®647
835 (Invitrogen cat.no. A32787, 1:500).

836 **Proximity ligation assay (PLA)**

837 Proximity ligation assay (PLA) was performed using the Duolink in situ red starter kit (Sigma-
838 Aldrich) following the manufacturer's instructions. Rabbit anti-RBM10 (Sigma-Aldrich
839 HPA034972, 1:2,000) and mouse anti-PCNA (Santa Cruz Bio cat. no. sc-56, 1:250) antibodies
840 were incubated for 1 hr at 37ºC prior to PLA analysis. PLA assay between RBM10 and EdU-
841 labelled nascent DNA was performed as previously described[94]. Briefly, cells were pulse
842 labelled with 100μM EdU for 10 min at 37ºC, followed by pre-extraction in 0.25% Triton X-
843 100 in PBS for 10 min on ice and fixation in 4% (wt/vol) paraformaldehyde. Cells were
844 incubated in EdU click reaction buffer containing 2mM CuSO4, 100mM ascorbic acid and

845 10μM biotin-azide (Invitrogen B10184) in PBS for 1 hr at room temperature. Cells were
846 incubated in blocking buffer for 1 hr at room temperature followed by incubation with rabbit
847 anti-RBM10 (Sigma-Aldrich HPA034972, 1:2000), rabbit anti-HDAC1 (GeneTex
848 GTX100513, 1:2,000), Rabbit anti-H4K16ac (Abcam ab109463, 1:2,000), rabbit anti-53BP1
849 (Novus biological NB100-305, 1:1,000) and mouse anti-biotin (Jackson ImmunoResearch
850 cat.no. 200-002-211, 1:2000) antibodies for 1 hr at 37°C. Next, PLA assay was performed using
851 the Duolink in situ red starter kit for experiments described in Fig. 3c,d (Sigma-Aldrich) or
852 NaveniFlex Cell MR Atto647N kit (Navinci) following the manufacturer's instructions.
853 Images were acquired using inverted Zeiss LSM-700 confocal microscope. Image analysis was
854 performed using ImageJ software. PLA intensity was calculated as the product of number of
855 spots and the mean intensity of the spots per nucleus.

856 **Cell synchronization**

857 To synchronize cells at G1/S border using double-thymidine block, cells were treated with
858 2 mM thymidine overnight, released for 10 h and treated again with thymidine overnight. Cells
859 were released into growth medium containing nocodazole (120 ng/ml) to enrich mitotic cells.
860 Cell cycle profiles were analyzed by Cytek Aurora© after staining with propidium iodide
861 (Sigma-Aldritch).

862 **Alkaline and neutral comet assays**

863 Alkaline and neutral comet assay was performed using the CometAssay Kit (Trevigen, 4250-
864 050-K) according to the manufacturer's instructions. Briefly, 1×10^5 cells/mL were mixed with
865 molten LMAgarose (at 37°C) at a ratio of 1:10 (v/v), and 70 μL of this mixture was transferred
866 onto a CometSlide. Slides were placed flat at 4°C in the dark for 30 minutes. Cells were then
867 lysed and subjected to alkaline or neutral electrophoresis with voltage of 1V/cm. DNA was
868 stained with SYBR green and slides were imaged using ZEISS LSM700 confocal microscope.
869 Comet tail moment was scored using CometScore 2.0 software.

870 **Short-term growth delay assay**

871 For determining drug sensitivity, cells were seeded in 96-well plates in duplicates at a density
872 of 2,000-5,000 cells per well. 24 hr post-seeding, drugs were added at the indicated
873 concentrations. Cell viability was measured 72 hr after drug treatment using the CellTiter 96®
874 AQueous One Solution Cell Proliferation Assay (Promega) following the manufacturer's
875 protocol, and absorbance was measured using Epoch Microplate Spectrophotometer (BioTek).
876 Cell viability was normalized to the viability of untreated cells.

877 **Clonogenic survival assays**

878 For colony survival assay, cells seeded onto 6-well plates (500 cells per well) and left untreated
879 or treated with the indicated doses of drugs. After 14 days, cells were fixed in methanol and
880 stained with 0.25% crystal violet. Individual colonies were counted, and relative survival was
881 calculated by normalizing to the number of colonies in control wells.

882 **Annexin-V apoptosis assay**

883 Apoptosis was assessed by annexin V-FITC kit (Invitrogen) according to the manufacturer's
884 instructions. Parental (WT) and RBM10-KO cells were treated with the indicated
885 concentrations of MK1775 for 24 hr prior to analysis. Samples (10,000 cells) were analyzed
886 using Cytek Aurora©. Results were calculated as the percentage of positive annexin V-FITC
887 cells out of total cells counted.

888 **Endogenous homologous recombination assay**

889 Homologous recombination repair assay was performed using Cas9-mediated knock-in of
890 green fluorescent mClover into the first exon of the LMNA gene, as previously described[69].
891 Briefly, cells were plated in 6-well plates and co-transfected with 1.6 µg pX330-LMNA-
892 gRNA1 plasmid containing Cas9 and gRNA against LMNA exon 1 and 0.4 µg pCR2.1-
893 CloverLamin plasmid containing HR donor sequence. In addition, 0.4 µg pDsRed-Monomer-
894 C1 was included per transfection as a transfection control unless otherwise indicated in the
895 figure legend. 12−16 h post transfection, culture medium was renewed and where indicated,
896 Caffeine (4 mM) was added. Seventy-two hours post-transfection, cells were collected and
897 analyzed by Cytek Aurora© . HR efficiency is percentage mClover-expressing cells from
898 DsRed-Monomer positive cells.

899 **DNA combing assays**

900 DNA combing analysis was performed as described[95]. Briefly, unsynchronized cells were pulse
901 labelled with 25uM Idu for 30 min, followed by 600µM CldU for another 30 min, followed by
902 1.5 hr growth without any label. For combing analysis with hydroxyurea (HU), cells were pulse
903 labelled with 25uM Idu for 30 min, followed by incubation with 4mM HU for 2 hr, followed
904 by pulse labelling 600µM CldU for another 30 min. Cells were harvested into 2% agarose
905 plugs, incubated for 48 hr in a digestion buffer (1% N Laurouylsarcosine, 0.2% Na
906 Deoxycholate, 10mM Tris-HCl pH 7.5, 100mM EDTA, and 1mg/ml proteinase K). Next, TE
907 50X was added overnight, and the plugs were dissolved into 50mM MES pH6 with 100mM
908 NaCl. The DNA was combed on Genomic vision combing slides, denatured and stained with
909 the following primary antibodies: Rat anti-BrdU (Abcam #ab6326, 1:200), mouse anti-BrdU
910 (BD Biosciences #347580, 1:20), and anti-ssDNA antibody (DSHB #AB10805144, 1:20). The

911 following secondary antibodies were used: Goat anti-mouse Alexa Fluor®647 (Jackson
912 Immunoresearch #115-605-166, 1:400), goat anti-rat Alexa Fluor®594 (ThermoFisher
913 Scientific #A11007, 1:400), and anti-mouse IgG2a Alexa Fluor®488 (ThermoFisher Scientific
914 #A21131, 1:500). The slides were photographed with a fluorescent microscope and analyzed
915 using Olympus CellSens program. For DNA combing analysis with S1 nuclease digestion, cells
916 were treated as indicated and then pulse labelled with 25uM Idu for 30 min, followed by 600µM
917 CldU for 60 min. Subsequently, cells were permeabilized (10 mM PIPES, pH 6.8, 0.1 M NaCl,
918 0.3 M sucrose, 3 mM MgCl2, EDTA-free Protease Inhibitor Cocktail (Roche)) at room
919 temperature for 10 min, followed by incubation with S1 nuclease (20 U/ml) (Promega M5761)
920 in S1 buffer for 60 min at 37 °C

921 **RNA sequencing**

922 Three biological replicates of RNA samples were purified from parental and RBM10-KO
923 HCC827 and H1299 cells, or HCC827 cells transfected with control or RBM10 siRNA#1.
924 RNA sequencing libraries were prepared using TruSeq mRNA library preparation kit.
925 Sequencing was performed at The Crown Genomics institute of the Nancy and Stephen Grand
926 Israel National Center for Personalized Medicine,Weizmann Institute of Science using a
927 NovaSeq 6000 system with S1 flow cell to obtain 150 bp paired-end reads. Average read depth
928 was 60 million reads per sample. The quality of the raw FASTQ files was assessed using
929 FastQC software (http://www.bioinformatics.babraham.ac.uk/projects/fastqc/). For differential
930 gene expression analysis, raw sequencing reads were aligned to GENCODE GRCh38 genome
931 assembly using Salmon package[96] and differential gene analysis was performed in R using the
932 DESeq2 package[97]. Pathway enrichment analysis and gene ontology was conducted using
933 ShinyGO[91].

934 **Mouse xenograft model**

935 Animal studies and protocols were approved by the Committee on the Ethics of Animal
936 Experiments of the Technion, Israel Institute of Technology (IL-069-07-22).
937 Immunocompromised NOD.CB17-Prkdcscid/NcrCrl (NOD SCID) mice were purchased from
938 Envigo. Mouse model of LUAD cell lines subcutaneous xenografts were established by
939 transplanting cells into 6-week-old female NOD SCID mice. Mice were randomly assigned
940 into control and treatment groups. Prior to initiating any experiments, mice were allowed one
941 week acclimation to housing conditions at the Technion Animal Facility. All mice were housed
942 in a strict pathogen-free environment. 2.5×10^6 of the indicated cells were resuspended in
943 100µl PBS and mixed 1:1 with Matrigel (High Concentration – Corning) and injected

944 subcutaneously into the right flank of 6 weeks-old female NOD SCID mice. Tumors were
945 measured using digital calipers. Tumor volumes were calculated using the formula: 0.5 × length
946 × width^2. When tumors reached ∼100mm^3, mice were randomly assigned to treatment groups
947 (n = 6 mice for each group, unless otherwise indicated). Each group received either control
948 (vehicle), MK1775 (40mg/kg, p.o.), or MK1775 + alisertib (30mg/kg each, p.o.) once daily for
949 15 days. Mice were euthanized when the tumors of control mice reached ∼1500mm^3 and
950 tumors were excised, weighed, and photographed.

951 **Immunohistochemistry**

952 Tumors excised from mice were fixed in 4% formalin at 4ºC overnight, washed three times
953 with PBS, and immersed in 30% (wt/vol) sucrose solution at 4ºC overnight. Then, tumors were
954 embedded in optimal cutting temperature compound (TissueTek) and frozen at -20ºC and.
955 10μm cryosections were prepared and permeabilized using 0.5% Triton X-100 in PBS followed
956 by immunofluorescence staining as described above, except primary antibody incubation with
957 γH2AX antibody (Millipore cat.no. 05-636,1:500) were performed at 4ºC overnight.

958 **Data availability**

959 Raw next-generation sequencing data for RBM10 SL CRISPR-Cas9 screen have been
960 deposited in ArrayExpress and are available through accession number E-MTAB-13626.
961 RNA-seq sequencing data generated in this study have been deposited in ArrayExpress
962 and are available through accession number E-MTAB-13617. The mass spectrometry
963 proteomics data have been deposited to the ProteomeXchange Consortium via the PRIDE
964 repository with the dataset identifier PXD040109. All data supporting the findings of this
965 study are available from the corresponding author upon request.

966

967 **References**

968 1. Sung, H. *et al.* Global Cancer Statistics 2020: GLOBOCAN Estimates of Incidence
969 and Mortality Worldwide for 36 Cancers in 185 Countries. *CA Cancer J Clin* **71**, 209–
970 249 (2021).
971 2. Siegel Mph, R. L. *et al.* Cancer statistics, 2023. *CA Cancer J Clin* **73**, 17–48 (2023).
972 3. Zappa, C. & Mousa, S. A. Non-small cell lung cancer: current treatment and future
973 advances. *Transl Lung Cancer Res* **5**, 288 (2016).
974 4. Herbst, R. S., Morgensztern, D. & Boshoff, C. The biology and management of non-
975 small cell lung cancer. *Nature 2018 553:7689* **553**, 446–454 (2018).
976 5. Collisson, E. A. *et al.* Comprehensive molecular profiling of lung adenocarcinoma.
977 *Nature 2014 511:7511* **511**, 543–550 (2014).
978 6. Zhang, S. *et al.* RNA binding motif protein 10 suppresses lung cancer progression by
979 controlling alternative splicing of eukaryotic translation initiation factor 4H.
980 *EBioMedicine* **61**, 103067 (2020).

981 7. Xie, M., Xu, X. & Fan, Y. KRAS-Mutant Non-Small Cell Lung Cancer: An Emerging
982 Promisingly Treatable Subgroup. *Front Oncol* **11**, 1535 (2021).
983 8. Cooper, A. J., Sequist, L. v. & Lin, J. J. Third-generation EGFR and ALK inhibitors:
984 mechanisms of resistance and management. *Nature Reviews Clinical Oncology 2022*
985 *19:8* **19**, 499–514 (2022).
986 9. Pio, R. & Montuenga, L. M. Alternative splicing in lung cancer. *J Thorac Oncol* **4**,
987 674–678 (2009).
988 10. Bonnal, S. C., López-Oreja, I. & Valcárcel, J. Roles and mechanisms of alternative
989 splicing in cancer — implications for care. *Nature Reviews Clinical Oncology 2020*
990 *17:8* **17**, 457–474 (2020).
991 11. Zhao, J. *et al.* Systematic profiling of alternative splicing signature reveals prognostic
992 predictor for prostate cancer. *Cancer Sci* **111**, 3020–3031 (2020).
993 12. Coomer, A. O., Black, F., Greystoke, A., Munkley, J. & Elliott, D. J. Alternative
994 splicing in lung cancer. *Biochim Biophys Acta Gene Regul Mech* **1862**, (2019).
995 13. de Fraipont, F., Gazzeri, S., Cho, W. C. & Eymin, B. Circular RNAs and RNA splice
996 variants as biomarkers for prognosis and therapeutic response in the liquid biopsies of
997 lung cancer patients. *Front Genet* **10**, (2019).
998 14. Cherry, S. & Lynch, K. W. Alternative splicing and cancer: insights, opportunities, and
999 challenges from an expanding view of the transcriptome. *Genes Dev* **34**, 1005–1016
1000 (2020).
1001 15. Li, Z. *et al.* The RNA-Binding Motif Protein Family in Cancer: Friend or Foe? *Front*
1002 *Oncol* **11**, (2021).
1003 16. Stanley, R. F. & Abdel-Wahab, O. Dysregulation and therapeutic targeting of RNA
1004 splicing in cancer. *Nat Cancer* **3**, 536–546 (2022).
1005 17. Machour, F. E. *et al.* RBM6 splicing factor promotes homologous recombination
1006 repair of double-strand breaks and modulates sensitivity to chemotherapeutic drugs.
1007 *Nucleic Acids Res* **49**, 11708–11727 (2021).
1008 18. Inoue, A., Takahashi, K. P., Kimura, M., Watanabe, T. & Morisawa, S. Molecular
1009 cloning of a RNA binding protein, S1-1. *Nucleic Acids Res* **24**, 2990–2997 (1996).
1010 19. Owczarek-Lipska, M., Markus, F., Bültmann, E., Korenke, G. C. & Neidhardt, J. A
1011 TARP Syndrome Phenotype Is Associated with a Novel Splicing Variant in RBM10.
1012 *Genes (Basel)* **13**, (2022).
1013 20. Daicheng, H., Shiwen, X., Jingxuan, Z., Junbo, H. & Bo, W. A Frameshift RBM10
1014 Variant Associated With TARP Syndrome. *Front Genet* **13**, (2022).
1015 21. Gebauer, F., Schwarzl, T., Valcárcel, J. & Hentze, M. W. RNA-binding proteins in
1016 human genetic disease. *Nat Rev Genet* **22**, 185–198 (2021).
1017 22. Højland, A. T. *et al.* First reported adult patient with TARP syndrome: A case report.
1018 *Am J Med Genet A* **176**, 2915 (2018).
1019 23. Imagawa, E., Konuma, T., Cork, E. E., Diaz, G. A. & Oishi, K. A novel missense
1020 variant in RBM10 can cause a mild form of TARP syndrome with developmental
1021 delay and dysmorphic features. *Clin Genet* **98**, 606–612 (2020).
1022 24. Gripp, K. W. *et al.* Long-term survival in TARP syndrome and confirmation of
1023 RBM10 as the disease-causing gene. *Am J Med Genet A* **155**, 2516–2520 (2011).
1024 25. Johnston, J. J. *et al.* Massively parallel sequencing of exons on the X chromosome
1025 identifies RBM10 as the gene that causes a syndromic form of cleft palate. *Am J Hum*
1026 *Genet* **86**, 743–748 (2010).
1027 26. Wang, Y. *et al.* Integrative analysis revealed the molecular mechanism underlying
1028 RBM10-mediated splicing regulation. *EMBO Mol Med* **5**, 1431–1442 (2013).
1029 27. Loiselle, J. J. & Sutherland, L. C. RBM10: Harmful or helpful-many factors to
1030 consider. *J Cell Biochem* **119**, 3809–3818 (2018).

1031 28. Rodor, J., FitzPatrick, D. R., Eyras, E. & Cáceres, J. F. The RNA-binding landscape of
1032 RBM10 and its role in alternative splicing regulation in models of mouse early
1033 development. *RNA Biol* **14**, 45–57 (2017).
1034 29. Dou, X. Q. *et al.* Alternative splicing of VEGFA is regulated by RBM10 in
1035 endometrial cancer. *Kaohsiung J Med Sci* **36**, 13–19 (2020).
1036 30. Inoue, A. *et al.* RBM10 regulates alternative splicing. *FEBS Lett* **588**, 942–947 (2014).
1037 31. Sutherland, L. C. *et al.* Splicing arrays reveal novel RBM10 targets, including SMN2
1038 pre-mRNA. *BMC Mol Biol* **18**, 1–14 (2017).
1039 32. Bechara, E. G., Sebestyén, E., Bernardis, I., Eyras, E. & Valcárcel, J. RBM5, 6, and 10
1040 differentially regulate NUMB alternative splicing to control cancer cell proliferation.
1041 *Mol Cell* **52**, 720–733 (2013).
1042 33. Yamada, H. *et al.* Src Family Tyrosine Kinase Signaling Regulates FilGAP through
1043 Association with RBM10. *PLoS One* **11**, (2016).
1044 34. Mohan, N., Kumar, V., Kandala, D. T., Kartha, C. C. & Laishram, R. S. A Splicing-
1045 Independent Function of RBM10 Controls Specific 3' UTR Processing to Regulate
1046 Cardiac Hypertrophy. *Cell Rep* **24**, 3539–3553 (2018).
1047 35. Kunimoto, H. *et al.* RBM10 regulates centriole duplication in HepG2 cells by
1048 ectopically assembling PLK4-STIL complexes in the nucleus. *Genes Cells* **25**, 100–
1049 110 (2020).
1050 36. Weigt, M. *et al.* Rbm10 facilitates heterochromatin assembly via the Clr6 HDAC
1051 complex. *Epigenetics Chromatin* **14**, (2021).
1052 37. Cao, Y. *et al.* RNA-binding motif protein 10 represses tumor progression through the
1053 Wnt/β- catenin pathway in lung adenocarcinoma. *Int J Biol Sci* **18**, 124–139 (2022).
1054 38. Inoue, A. RBM10: Structure, functions, and associated diseases. *Gene* **783**, (2021).
1055 39. Hernández, J. *et al.* Tumor suppressor properties of the splicing regulatory factor
1056 RBM10. *RNA Biol* **13**, 466–472 (2016).
1057 40. Atsumi, T. *et al.* Rbm10 regulates inflammation development via alternative splicing
1058 of Dnmt3b. *Int Immunol* **29**, 581–591 (2017).
1059 41. Xiao, W. *et al.* RBM10 regulates human TERT gene splicing and inhibits pancreatic
1060 cancer progression. *Am J Cancer Res* **11**, 157 (2021).
1061 42. Cao, Y. *et al.* RBM10 recruits METTL3 to induce N6-methyladenosine-MALAT1-
1062 dependent modification, inhibiting the invasion and migration of NSCLC. *Life Sci* **315**,
1063 (2023).
1064 43. Jin, X. *et al.* RBM10 inhibits cell proliferation of lung adenocarcinoma via
1065 RAP1/AKT/CREB signalling pathway. *J Cell Mol Med* **23**, 3897–3904 (2019).
1066 44. Jung, J. H. *et al.* RNA-binding motif protein 10 induces apoptosis and suppresses
1067 proliferation by activating p53. *Oncogene* **39**, 1031–1040 (2020).
1068 45. Wang, Y. *et al.* Distinct gene mutation profiles among multiple and single primary
1069 lung adenocarcinoma. *Front Oncol* **12**, 6746 (2022).
1070 46. Vinayanuwattikun, C. *et al.* Elucidating Genomic Characteristics of Lung Cancer
1071 Progression from In Situ to Invasive Adenocarcinoma. *Scientific Reports 2016 6:1* **6**,
1072 1–10 (2016).
1073 47. Chen, H. *et al.* Genomic and immune profiling of pre-invasive lung adenocarcinoma.
1074 *Nat Commun* (2019) doi:10.1038/s41467-019-13460-3.
1075 48. Seiler, M. *et al.* Somatic Mutational Landscape of Splicing Factor Genes and Their
1076 Functional Consequences across 33 Cancer Types. *Cell Rep* (2018)
1077 doi:10.1016/j.celrep.2018.01.088.
1078 49. Rao, W. *et al.* Frequently mutated genes in predicting the relapse of stage I lung
1079 adenocarcinoma. *Clin Transl Oncol* (2023) doi:10.1007/S12094-023-03074-Z.

1080 50. Zhao, J. *et al.* Functional analysis reveals that RBM10 mutations contribute to lung
1081 adenocarcinoma pathogenesis by deregulating splicing. *Sci Rep* **7**, (2017).
1082 51. Nanjo, S. *et al.* Deficiency of the splicing factor RBM10 limits EGFR inhibitor
1083 response in EGFR-mutant lung cancer. *J Clin Invest* **132**, (2022).
1084 52. Hart, T. *et al.* High-Resolution CRISPR Screens Reveal Fitness Genes and Genotype-
1085 Specific Cancer Liabilities. *Cell* (2015) doi:10.1016/j.cell.2015.11.015.
1086 53. Hart, T. & Moffat, J. BAGEL: a computational framework for identifying essential
1087 genes from pooled library screens. *BMC Bioinformatics* **17**, (2016).
1088 54. Li, W. *et al.* MAGeCK enables robust identification of essential genes from genome-
1089 scale CRISPR/Cas9 knockout screens. *Genome Biol* **15**, 554 (2014).
1090 55. Adam, S. *et al.* The CIP2A–TOPBP1 axis safeguards chromosome stability and is a
1091 synthetic lethal target for BRCA-mutated cancer. *Nature Cancer 2021 2:12* **2**, 1357–
1092 1371 (2021).
1093 56. Kavanaugh, G. *et al.* A whole genome RNAi screen identifies replication stress
1094 response genes. *DNA Repair (Amst)* **35**, 55–62 (2015).
1095 57. Matsuoka, S. *et al.* ATM and ATR substrate analysis reveals extensive protein
1096 networks responsive to DNA damage. *Science (1979)* (2007)
1097 doi:10.1126/science.1140321.
1098 58. Weinstein, J. N. *et al.* The Cancer Genome Atlas Pan-Cancer analysis project. *Nat*
1099 *Genet* **45**, 1113–1120 (2013).
1100 59. Nguyen, C. D. *et al.* Characterization of a Family of RanBP2-Type Zinc Fingers that
1101 Can Recognize Single-Stranded RNA. *J Mol Biol* **407**, 273–283 (2011).
1102 60. Collins, K. M. *et al.* An RRM–ZnF RNA recognition module targets RBM10 to exonic
1103 sequences to promote exon exclusion. *Nucleic Acids Res* **45**, 6761–6774 (2017).
1104 61. Leriche, M. *et al.* 53BP1 interacts with the RNA primer from Okazaki fragments to
1105 support their processing during unperturbed DNA replication. *Cell Rep* **42**, 113412
1106 (2023).
1107 62. Agudelo Garcia, P. A. *et al.* Histone acetyltransferase 1 is required for DNA
1108 replication fork function and stability. *Journal of Biological Chemistry* **295**, 8363–
1109 8373 (2020).
1110 63. Kehrli, K. *et al.* Class i histone deacetylase HDAC1 and WRN RECQ helicase
1111 contribute additively to protect replication forks upon hydroxyurea-induced arrest.
1112 *Journal of Biological Chemistry* **291**, 24487–24503 (2016).
1113 64. Bhaskara, S. *et al.* Histone deacetylases 1 and 2 maintain S-phase chromatin and DNA
1114 replication fork progression. *Epigenetics Chromatin* **6**, 1–22 (2013).
1115 65. Gaggioli, V. *et al.* Dynamic de novo heterochromatin assembly and disassembly at
1116 replication forks ensures fork stability. *Nature Cell Biology 2023 25:7* **25**, 1017–1032
1117 (2023).
1118 66. de Vivo, A. *et al.* OTUD5 limits replication fork instability by organizing chromatin
1119 remodelers. *Nucleic Acids Res* **51**, 10467–10483 (2023).
1120 67. Ait Saada, A., Lambert, S. A. E. & Carr, A. M. Preserving replication fork integrity
1121 and competence via the homologous recombination pathway. *DNA Repair (Amst)* **71**,
1122 135–147 (2018).
1123 68. Chakraborty, S., Schirmeisen, K. & Lambert, S. A. The multifaceted functions of
1124 homologous recombination in dealing with replication-associated DNA damages. *DNA*
1125 *Repair (Amst)* **129**, 103548 (2023).
1126 69. Pinder, J., Salsman, J. & Dellaire, G. Nuclear domain 'knock-in' screen for the
1127 evaluation and identification of small molecule enhancers of CRISPR-based genome
1128 editing. *Nucleic Acids Res* **43**, 9379–9392 (2015).

1129 70. Ghelli Luserna Di Rorà, A., Cerchione, C., Martinelli, G. & Simonetti, G. A WEE1
1130 family business: regulation of mitosis, cancer progression, and therapeutic target. *J*
1131 *Hematol Oncol* **13**, (2020).
1132 71. Elbæk, C. R., Petrosius, V. & Sørensen, C. S. WEE1 kinase limits CDK activities to
1133 safeguard DNA replication and mitotic entry. *Mutation Research/Fundamental and*
1134 *Molecular Mechanisms of Mutagenesis* **819–820**, 111694 (2020).
1135 72. Elbæk, C. R. *et al.* WEE1 kinase protects the stability of stalled DNA replication forks
1136 by limiting CDK2 activity. *Cell Rep* **38**, (2022).
1137 73. Bukhari, A. B., Chan, G. K. & Gamper, A. M. Targeting the DNA Damage Response
1138 for Cancer Therapy by Inhibiting the Kinase Wee1. *Front Oncol* **12**, 347 (2022).
1139 74. da Costa, A. A. B. A., Chowdhury, D., Shapiro, G. I., D'Andrea, A. D. &
1140 Konstantinopoulos, P. A. Targeting replication stress in cancer therapy. *Nat Rev Drug*
1141 *Discov* **22**, 38–58 (2023).
1142 75. Hirai, H. *et al.* Small-molecule inhibition of Wee1 kinase by MK-1775 selectively
1143 sensitizes p53-deficient tumor cells to DNA-damaging agents. *Mol Cancer Ther* **8**,
1144 2992–3000 (2009).
1145 76. Cong, K. *et al.* Replication gaps are a key determinant of PARP inhibitor synthetic
1146 lethality with BRCA deficiency. *Mol Cell* **81**, 3128-3144.e7 (2021).
1147 77. Kong, A. & Mehanna, H. WEE1 Inhibitor: Clinical Development. *Curr Oncol Rep* **23**,
1148 (2021).
1149 78. Coulombe, P. *et al.* The ORC ubiquitin ligase OBI1 promotes DNA replication origin
1150 firing. *Nature Communications 2019 10:1* **10**, 1–14 (2019).
1151 79. Giansanti, C. *et al.* MDM2 binds and ubiquitinates PARP1 to enhance DNA
1152 replication fork progression. *Cell Rep* **39**, 110879 (2022).
1153 80. Aliyaskarova, U. *et al.* NEIL3-mediated proteasomal degradation facilitates the repair
1154 of cisplatin-induced DNA damage in human cells. *Sci Rep* **13**, (2023).
1155 81. Vujanovic, M. *et al.* Replication Fork Slowing and Reversal upon DNA Damage
1156 Require PCNA Polyubiquitination and ZRANB3 DNA Translocase Activity. *Mol Cell*
1157 **67**, 882-890.e5 (2017).
1158 82. Jia, W. *et al.* Fused in sarcoma regulates DNA replication timing and kinetics. *J Biol*
1159 *Chem* **297**, (2021).
1160 83. Lee, J. W. *et al.* Combined Aurora Kinase A (AURKA) and WEE1 Inhibition
1161 Demonstrates Synergistic Antitumor Effect in Squamous Cell Carcinoma of the Head
1162 and Neck. *Clin Cancer Res* **25**, 3430–3442 (2019).
1163 84. Zheng, H., Shao, F., Martin, S., Xu, X. & Deng, C. X. WEE1 inhibition targets cell
1164 cycle checkpoints for triple negative breast cancers to overcome cisplatin resistance.
1165 *Sci Rep* **7**, (2017).
1166 85. Chen, D. *et al.* Wee1 Inhibitor AZD1775 Combined with Cisplatin Potentiates
1167 Anticancer Activity against Gastric Cancer by Increasing DNA Damage and Cell
1168 Apoptosis. *Biomed Res Int* **2018**, (2018).
1169 86. Aarts, M. *et al.* Forced mitotic entry of S-phase cells as a therapeutic strategy induced
1170 by inhibition of WEE1. *Cancer Discov* **2**, 524–539 (2012).
1171 87. Rajeshkumar, N. V. *et al.* MK-1775, a potent Wee1 inhibitor, synergizes with
1172 gemcitabine to achieve tumor regressions, selectively in p53-deficient pancreatic
1173 cancer xenografts. *Clin Cancer Res* **17**, 2799–2806 (2011).
1174 88. Liu, B. *et al.* RBM10 Deficiency Is Associated With Increased Immune Activity in
1175 Lung Adenocarcinoma. *Front Oncol* **11**, 677826 (2021).
1176 89. Awwad, S. W., Serrano-Benitez, A., Thomas, J. C., Gupta, V. & Jackson, S. P.
1177 Revolutionizing DNA repair research and cancer therapy with CRISPR-Cas screens.
1178 *Nat Rev Mol Cell Biol* (2023) doi:10.1038/S41580-022-00571-X.

90. Gallo, D. *et al.* CCNE1 amplification is synthetic lethal with PKMYT1 kinase inhibition. *Nature 2022 604:7907* **604**, 749–756 (2022).
91. Ge, S. X., Jung, D., Jung, D. & Yao, R. ShinyGO: a graphical gene-set enrichment tool for animals and plants. *Bioinformatics* **36**, 2628–2629 (2020).
92. Khoury-Haddad, H. *et al.* PARP1-dependent recruitment of KDM4D histone demethylase to DNA damage sites promotes double-strand break repair. *Proc Natl Acad Sci U S A* **111**, (2014).
93. Cox, J. & Mann, M. MaxQuant enables high peptide identification rates, individualized p.p.b.-range mass accuracies and proteome-wide protein quantification. *Nature Biotechnology 2008 26:12* **26**, 1367–1372 (2008).
94. Roy, S., Luzwick, J. W. & Schlacher, K. SIRF: Quantitative in situ analysis of protein interactions at DNA replication forks. *Journal of Cell Biology* **217**, 1521–1536 (2018).
95. Kaykov, A., Taillefumier, T., Bensimon, A. & Nurse, P. Molecular Combing of Single DNA Molecules on the 10 Megabase Scale. *Scientific Reports 2016 6:1* **6**, 1–9 (2016).
96. Patro, R., Duggal, G., Love, M. I., Irizarry, R. A. & Kingsford, C. Salmon provides fast and bias-aware quantification of transcript expression. *Nature Methods 2017 14:4* **14**, 417–419 (2017).
97. Love, M. I., Huber, W. & Anders, S. Moderated estimation of fold change and dispersion for RNA-seq data with DESeq2. *Genome Biol* **15**, 1–21 (2014).